Development and Validation of Improved Techniques for Cloud Property Retrieval from Environmental Satellites

Gary B. Gustafson
Robert P. d'Entremont

Atmospheric and Environmental Research, Inc.
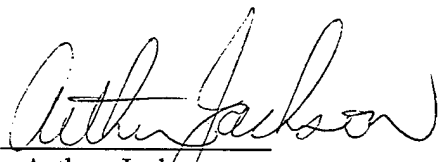131 Hartwell Ave
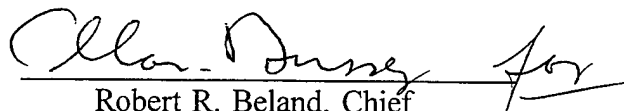Lexington, MA 02421

17 Nov 2000

Final Report

20011031 146

AIR FORCE RESEARCH LABORATORY
Space Vehicles Directorate
29 Randolph Rd
AIR FORCE MATERIEL COMMAND
Hanscom AFB, MA 01731-3010

This Technical Report has been reviewed and is approved for publication.

Arthur Jackson
Contract Manager

Robert R. Beland, Chief
Tactical Environmental Support Branch

REPORT DOCUMENTATION PAGE

1. REPORT DATE *(DD-MM-YYYY)*	2. REPORT TYPE	3. DATES COVERED *(From - To)*
17-11-2000	Scientific, Final	

4. TITLE AND SUBTITLE
Development and Validation of Improved Techniques for Cloud Property Retrieval from Environmental Satellites

5a. CONTRACT NUMBER
F19628-96-C-0053

5b. GRANT NUMBER

5c. PROGRAM ELEMENT NUMBER
62601F

6. AUTHOR(S)
Gary B. Gustafson
Robert P. d'Entremont

5d. PROJECT NUMBER
6670

5e. TASK NUMBER
GT

5f. WORK UNIT NUMBER
FD

7. PERFORMING ORGANIZATION NAME(S) AND ADDRESS(ES)
Atmospheric and Environmental Research, Inc.
131 Hartwell Ave
Lexington, MA 02421

8. PERFORMING ORGANIZATION REPORT NUMBER
P688

9. SPONSORING/MONITORING AGENCY NAME(S) AND ADDRESS(ES)
Air Force Research Laboratory
29 Randolph Rd
Hanscom AFB, MA 01731-3010

10. SPONSOR/MONITOR'S ACRONYM(S)

11. SPONSOR/MONITOR'S REPORT NUMBER(S)
AFRL-VS-TR-2001-1549

12. DISTRIBUTION/AVAILABILITY STATEMENT
Approved for Public Release; distribution unlimited.

13. SUPPLEMENTARY NOTES

14. ABSTRACT
A basic research program was conducted for the Air Force Research Laboratory, consisting of three tasks: 1) develop extensible cloud property retrieval algorithms suitable for expanding existing cloud analysis capabilities to utilize data from new and future environmental satellite sensing systems; 2) develop advanced algorithms for retrieval of cloud properties that are insufficiently resolved to satisfy Air Force requirements using existing techniques; and 3) validate cloud property retrieval algorithms using real data from existing meteorological satellite platforms. Under task 1 a series of algorithms developed under previous AFRL programs were modified to expand capabilities in several areas including improved transmissive cirrus detection and classification, cloud phase retrieval, snow/cloud discrimination, and transition across the terminator. In task 2 new capabilities were developed to retrieve cloud radiative and microphysical properties from multispectral data available from environmental satellites including the newly launched MODIS. Under task 3 the new algorithms were implemented in software and applied to real data acquired from the GOES 8 satellite in support of two field programs conducted or supported by AFRL.

15. SUBJECT TERMS
Cloud physics   Meteorological satellites   Algorithms

16. SECURITY CLASSIFICATION OF:			17. LIMITATION OF ABSTRACT	18. NUMBER OF PAGES	19a. NAME OF RESPONSIBLE PERSON
a. REPORT	b. ABSTRACT	c. THIS PAGE			Arthur Jackson/VSBL
UNCL	UNCL	UNCL	UNL	50	19b. TELEPHONE NUMBER *(Include area code)* (781) 377-2958

Table of Contents

List of Figures

List of Tables

1. Introduction

Existing and planned objective cloud analysis capabilities at the Air Force Weather Agency (AFWA) make use of multispectral data from multiple satellite systems. However in a number of important areas, gaps or weakness exist in the analysis methodology that affect the ability to adequately address Air Force requirements: 1) quantitative interpretation of daytime sensor channel data in the visible to midwave-infrared (MWIR) spectrum; 2) detection and discrimination of transmissive cirrus; 3) accurate cloud height assignment due to incomplete modeling of microphysical and radiative properties; 4) use of remotely sensed cloud radiative and environment characteristics to improve retrieval accuracy for cloud altitude; and 5) use of inferred cloud physical characteristics to provide temporal consistency across the day/night terminator.

This report describes a three-task basic research effort conducted for the Air Force Research Laboratory designed to address the weakness described above. Under task 1 a set of existing cloud analysis algorithms developed under a series of previous studies conducted for AFRL were expanded to exploit new capabilities available from recently launched environmental satellite imaging sensors. These include the imaging sensor on board the Geostationary Operational Environmental Satellites (GOES) in the series designated I-M, the Advanced Very High Resolution Radiometer (AVHRR), version 3, and the Moderate Resolution Imaging Spectroradiometer (MODIS). New capabilities include improved detection and classification of optically thin cirrus and low stratus; cloud phase retrieval; discrimination of cloud over reflective backgrounds such as snow, desert and sun glint; and transition across the terminator. In task 2 new capabilities were developed to accurately retrieve cloud radiative and microphysical properties using multispectral imager data. This information is then used to provide improved estimations of cloud top altitude. Task 3 consisted of implementing the new algorithms in software and testing them on real meteorological satellite data. The principal data source was the GOES 8 imager. Two multi-day data sets were collected over New England and Florida in 1995 and 1996, respectively, in support of AFRL conducted/supported field programs for investigation of contrail formation.

2. Cloud Analysis

This section describes a set of multispectral algorithms developed for detection and phase classification of cloud from remotely sensed radiometer measurements in the visible to infrared. Emphasis was on development of techniques compatible with existing or planned environmental satellite platforms. The report provides background information on the heritage and scientific basis of each algorithm, the sensor and supporting database requirements, and a description of how the algorithms were implemented in software.

The overall algorithm structure is that of a multispectral decision tree, an approach that has been successfully used by numerous investigators including Saunders and Kriebel (1988), Kaarlson and Lilhas (1990), Ackerman et al. (1998), and Stowe et al. (1999). AER also successfully used this approach on two previous cloud analysis programs undertaken for the U. S. Air Force that together formed much of the heritage of these algorithms. The first was development of a set of autonomous, relocatable, regional cloud detection algorithms for use on in-theater tactical satellite ground stations using only direct broadcast data from polar-orbiting environmental satellites (Gustafson et al., 1996). These algorithms, collectively known as TACNEPH (for tactical nephanalysis),

are currently listed as Incremental Technology Insertion items for the operational Small Tactical Terminal system. The second Air Force effort was development of a series of algorithms to perform global cloud detection and retrieval of cloud spatial properties using the full resources of a major forecast center. These algorithms analyze multi source imaging-sensor data from the Defense Meteorological Satellite Program (DMSP), the Television Infrared Observing System (TIROS), and the international constellation of geostationary satellites (Gustafson et al., 1994 and 1997). They were subsequently selected for operational implementation at the Air Force Weather Agency (AFWA) as part of an overall upgrade of the AFWA satellite-data processing environment under the Cloud Depiction and Forecast System II (CDFS II) program (Gustafson et al., 1997 and 2000). CDFS II is scheduled to go online in 2001 replacing the currently operational RTNEPH model.

The cloud algorithms described in this document build on the TACNEPH and CDFS II heritage by adding new capabilities specifically designed to address known weaknesses of the earlier AVHRR-, DMSP-, and GEO-based algorithms. Specifically new development addressed the following: difficulty in detecting and correctly classifying optically thin cirrus; misclassification of cloud over reflective backgrounds such as snow/ice, desert, sun glint; poor discrimination of cloud that is thermally indistinct from the terrestrial background, particularly at night; and detection of small-scale cloud over ocean surfaces. In addition, an improved capability to discriminate cloud phase was developed to address requirements imposed by the cloud property retrieval algorithms described in Section 3.

The cloud algorithms described in this document have the following characteristics:

- evaluate results of multiple independent tests each designed to analyze a specific cloud or background signature in the multispectral sensor data;

- analyze satellite data as the primary input and minimize requirements for supporting data such as surface temperature estimates, temperature and moisture profiles from Numerical Weather Prediction (NWP) model products, and fixed terrain, eco-system, and geography databases; and

- incorporate lessons learned from numerous heritage programs and expand their capabilities to address known weaknesses.

2.1 Cloud Detection Algorithm Description

Cloud detection is performed through analysis of multispectral data obtained from available satellite sensors including the GOES imager, AVHRR-3, and MODIS. Supporting datasets derived from either remote sensing or other sources are also required to provide estimates of the clear-scene radiative characteristics of the terrestrial background and the atmosphere. The sensor channel wavelengths used by the cloud algorithms are listed in Table 1. The algorithms exploit differences in the wavelength-dependent reflection, emission and transmission characteristics exhibited by cloud and terrestrial surfaces to classify a scene.

Various techniques to evaluate spectral signatures for the presence of cloud are used in the algorithms. In this application spectral signatures are defined as any distinctive and identifiable characteristic in the available sensor and supporting data that can be used to classify a pixel location as either cloud or clear. For example, the reflectance and emittance characteristics of many surfaces exhibit wavelength dependencies as illustrated

Table 1 Sensor channel wavelengths used by the cloud algorithms

Wavelength (μm)	Designation[1]	GOES Imager	AVHRR	MODIS	Calibrated Quantity[2]
0.65	VIS	√	√	√	reflectance
0.85	NIR		√	√	reflectance
1.38	SWIR			√	reflectance
1.60	SWIR		√	√	reflectance
3.70 – 3.90	MWIR	√	√	√	EBBT
6.70 – 7.00	WV	√		√	EBBT
8.55	LWIR			√	EBBT
10.8	LWIR	√	√	√	EBBT
12.00	LWIR	√	√	√	EBBT

[1]Wavelength Designation: VIS – visible; NIR – near infrared; SWIR – short wave infrared; MWIR – mid wave infrared; WV – water vapor absorption channel; LWIR – long wave infrared.

[2]EBBT: Equivalent Blackbody Brightness Temperature computed by inverting the Planck function at the sensor wavelength for the satellite-measured radiance.

in Figure 1. As a consequence, comparison of sensor measurements at multiple wavelengths is a commonly used technique to classify the surface being observed. Other useful signatures include contrast between cloud and the cloud-free background in one or more spectral bands and comparisons between the spectral information in the satellite data and estimates of the radiative characteristics of the underlying terrestrial surface inferred from supporting data (e.g., geography or ecosystem type). A suite of tests has been developed to classify the different spectral characteristics exhibited by clouds and background surfaces as either clear or cloudy. Each test is based on one or more spectral signatures that exploit the information content of radiance measurements from one or more of the nine sensor channels identified in Table 1.
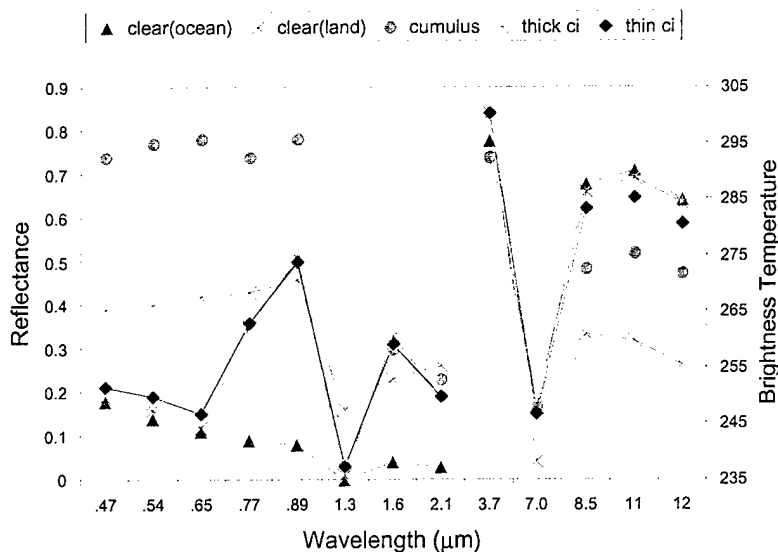
Figure 1 Wavelength dependence of the reflectance and emittance characteristics of some common clouds and terrestrial surfaces

The tests used to evaluate spectral signatures in the data are summarized in Table 2. The tests fall into two categories, cloud tests and background tests. As indicated by the test names and descriptions, different tests are used to identify specific pixel characteristics under defined conditions. For example, the Low Cloud and Fog Test for Solar-Illuminated Data is used to identify liquid water phase, thermally indistinct low cloud when the scene is solar-illuminated. The Low Cloud and Fog Test for Non-Solar-Illuminated Data is used when the scene is on the night side of the terminator. Note that test names are used for identification only. Typically cloud-test names indicate only the primary class the test was designed to identify while in practice individual tests frequently also identify other types of cloud or background in addition to that indicated by the name. Background tests (identified in Table 2) are designed to identify spectral signatures from cloud-free surfaces that are similar in at least one characteristic to cloud. These are necessary to avoid the incorrect classification by one or more cloud tests that are sensitive to those clear-scene spectral signatures. External data sources, such as land-type classifications, NWP models, and snow cover databases, are also used to identify problematic backgrounds, however they are only used to supplement the spectral tests which are generally more timely and of higher spatial resolution.

Table 2 Cloud detection tests

	Test Name	Day	Night	Major Identification Class
Cloud Tests	Stratus, Low Cloud and Fog	√	√	Daytime and nighttime versions for liquid water phase cloud
	Precipitating Cloud Test	√		Deep convective cloud
	MWIR-LWIR Thin Cirrus	√	√	Daytime and nighttime versions for transmissive cirrus cloud
	NIR Thin Cirrus	√		Mid- to high-level cloud and very transmissive cirrus
	NIR/Visible Reflectance Ratio	√		Daytime liquid water phase cloud
	Single Channel Reflectance	√		Daytime liquid water phase cloud
	LWIR Threshold	√	√	Mid- to high-altitude optically thick water and ice cloud
	LWIR Cirrus Cloud	√	√	High-altitude ice cloud
	Water Vapor	√	√	Mid- to high-altitude cloud and black stratus[1]
	Cloud Phase	√	√	Liquid/ice phase determination
Background Tests	Sun Glint Background Test	√		Water surfaces exhibiting specular reflection
	Desert Background Test	√		Highly reflective non-vegetated land surfaces
	Snow/Ice Cover Background Test	√		Highly reflective snow or ice covered land and water surfaces

[1] Black stratus refers to the condition most commonly found in polar regions where status cloud forms below a surface inversion wherein the temperature of the cloud is greater than the that of the terrestrial background. The name black comes the way from these clouds appear when imagery is viewed using the common visualization technique that codes brightness temperatures as shades of gray with lower temperatures as white and warm as black.

4

The decision tree structure of the cloud detection algorithms controls which tests from Table 2 the multispectral pixel data are subjected to based on the background, view and illumination conditions at the pixel location. Since individual tests are sensitive to specific conditions it is not expected that any one test will identify all cloud in a scene. Some tests require the results of other tests to make a cloud determination. For example, background tests are used to either modify affected cloud tests or eliminate the use of certain channel data from the analysis process. As successive tests are executed and individual results obtained, more information on the total cloud environment is compiled. When all applicable tests have been run the final cloud determination is made by jointly evaluating the results of all tests. A consequence of the graceful degradation capability designed into the algorithm is the inclusion of logic in each test to determine whether required sensor and supporting data are available.

2.2 Scientific Basis

The following sections provide background and the scientific basis for the cloud/background detection and classification tests used at each branch of the decision tree algorithm. As stated above, the individual cloud tests that make up the cloud cover algorithm evaluate spectral signatures in the radiance data and the supporting information describing the background and atmospheric characteristics. Table 1 lists the channel wavelengths used by the algorithm. These channels were selected because their radiative characteristics respond in predictable ways to the presence of cloud or specific types of backgrounds. For channel wavelengths below 3.0 μm measured radiance at the sensor is primarily reflected solar, above 4.0 μm the principal component is emitted energy, and between 3.0 and 4.0 μm both reflected solar and emitted energy contribute.

2.2.1 Reflectance Channels

Reflectance properties of different surfaces vary with wavelength between the visible and NIR. Figure 2 illustrates how reflectance varies for vegetated land, water, ice/snow, desert, liquid water cloud and ice cloud. These spectral dependencies are exploited by the cloud tests to identify cloud and discriminate them from various backgrounds. Note from the figure that water surfaces are poor reflectors in all bands while vegetated land reflects preferentially at 0.85 μm. Ice and snow surfaces have high reflectance at 0.65 and 0.85 μm but relatively low values at 1.6 μm. Clouds tend to reflect well at all wavelengths except ice-phase cloud at 1.6 μm. Note that between 0.65 and 0.85 μm, cloud reflectance exhibits very little spectral dependency. In addition to cloud, atmospheric constituents also impact measured top of atmosphere (TOA) reflectance at 0.65 μm and 1.38 μm. Note that water surfaces exhibit a visible reflectance that is slightly greater than in the near infrared (NIR) due to greater scattering from small marine aerosol and haze droplets than at the shorter wavelength. At 1.38 μm, very little energy from the surface is received at the satellite due to strong absorption by atmospheric water vapor in that channel.
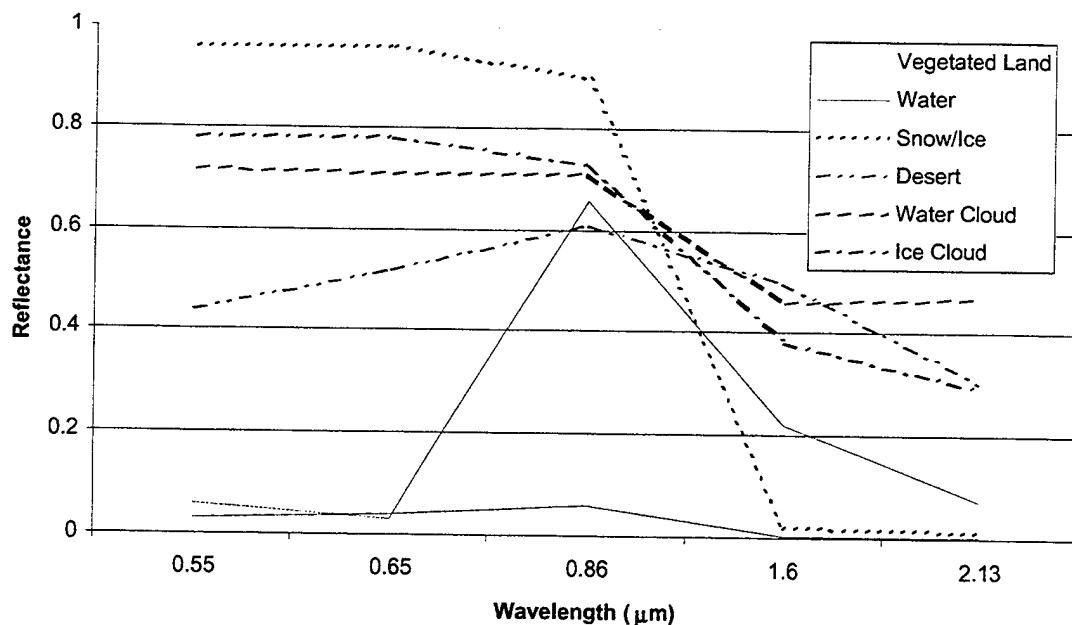
Figure 2 Reflectance of various surfaces in visible to near infrared wavelengths

2.2.2 Emittance Channels

From Table 1 it can be seen that IR channels at 6.7, 8.55, 10.8 and 12.0 μm are used by the cloud algorithm. At these wavelengths reflectance of cloud and background surfaces of interest to this application are negligible. Thus upwelling energy measured at the satellite sensor is dominated by the emissivity/transmissivity of an emitting surface, the transmission of the atmosphere, the temperature of the surface and, for transmissive cloud, the temperature of the underlying surface. Figure 3 illustrates that the 8.55, 10.8 and 12.0 μm channels all lie in window regions of the atmosphere, while the 6.7 μm channel is in a strong water vapor absorption region.

Of the window channels, 12.0 μm is most impacted by atmospheric water vapor and comparisons of 10.8 − 12.0 μm brightness temperatures under cloud-free conditions confirm this through a low bias at the longer wavelengths. When ice clouds are present, the magnitude of the 10.8 − 12.0 μm brightness temperature difference increases due to greater absorption by ice particles at 12.0 μm. Similarly, in the 8.55 to 10.8 μm region Mie theory predicts, and observations confirm (Takano et al., 1992), that absorption by ice particles also increases with wavelength and dependence on atmospheric water vapor is roughly equal at both wavelengths. Thus under cloud-free conditions 8.55 − 10.8 μm brightness temperature differences will be near zero and smaller than for 10.8 − 12.0 μm (due to lower atmospheric transmission at 12.0) while for ice clouds they will be greater. Strabala et al. (1994) demonstrated that for liquid water clouds the situation is reversed. Absorption by small water droplets between 8.55 and 10.8 μm is roughly constant and then increases rapidly at 12.0 μm. Thus brightness temperature differences between 8.55 and 10.8 μm will be less than between 10.8 and 12.0 μm.

6

At 6.7 μm, strong water vapor absorption insures that for all but the driest atmospheres the channel weighting function will peak above the Earth surface. As the total column water vapor increases, or as the distribution of water vapor in the atmosphere moves upward, the radiating temperature measured at 6.7 μm becomes representative of the air higher in the atmosphere. For mid-latitude and tropical regions this results in a strong negative clear-scene brightness temperature differences between 6.7 – 10.8 μm (10.8 selected for comparison as the cleanest window channel). In very dry polar regions the 6.7 μm channel brightness temperature can be representative of the air temperature just above the boundary layer. In situations of strong temperature inversions this can result in a positive 6.7 – 10.8 μm temperature difference.

Figure 3 Atmospheric transmittance in mid to long wave infrared wavelengths

2.2.3   Midwave Infrared Channel

At 3.9 μm, energy measured at the sensor aperture can be either reflected solar or emitted. This unique characteristic, coupled with the optical properties of clouds at this wavelength, is very useful for detecting clouds that have either weak or ambiguous spectral signatures at the other wavelengths.

Low level clouds, particularly marine stratus and fog, are generally composed of small water droplets. Mie theory predicts that in the midwave IR scattering by small water droplets is strongly dependent on drop size. For cloud with drop sizes between 4 and 10 μm the TOA reflectance will vary from approximately 0.35 to 0.15. Assuming an opaque cloud (i.e., $\rho + \varepsilon \cong 1$) and neglecting atmospheric effects, the TOA radiance will be a weighted combination of the emitted and reflected components:

$$I_{obs} = (1-\rho) \ B(T_{cld}) + \rho \ (B(T_{sol}) \ (E_{rad}/D)^2 \ cos(\theta) \qquad \text{Eq. 1}$$

where: I_{obs} is the TOA radiance measured at the sensor, ρ the cloud reflectance, $B(T_{cld})$ the Planck radiance of the cloud temperature, $B(T_{sol})$ the Planck radiance of the Sun, E_{rad} Earth radius, D the mean Earth-Sun distance, and θ the solar zenith angle. At night, Eq. 1 becomes:

$$I_{obs} = \varepsilon \ B(T_{cld})$$

<div align="right">Eq. 2</div>

This results in computed brightness temperatures in the MWIR that are greater than true cloud temperature during the day and nighttime temperatures that are less. Table 3 provides a list of 3.9 μm daytime brightness temperatures consistent with two water clouds with particle sizes of 4 and 10 μm for a range of solar angles and true cloud temperatures. Table 4 provides the same information for nighttime cases.

Table 3 Daytime 3.9 μm brightness temperature dependence on cloud temperature, reflectivity and solar angle from Eq. 1

Reflectivity	Solar Angle	Cloud Temperature			
		300	280	260	250
0.15	0	313	303	298	297
	30	311	301	295	294
	60	305	293	285	283
0.35	0	324	320	317	317
	30	321	316	314	313
	60	312	304	301	300

Table 4 Nighttime 3.9 μm brightness temperature dependence on cloud temperature and emissivity from Eq. 2

Emissivity	Cloud Temperature			
	300	280	260	250
0.85	296	277	257	247
0.65	290	271	252	243

The implications for using the 3.9 μm channel together with the 10.8 and 12.0 μm channels for nighttime detection of transmissive cirrus cloud are also significant. In this case cloud transmission is non-zero and the ice cloud reflectance is assumed to be negligible (i.e. $\tau + \varepsilon \cong 1$). Thus the upwelling TOA radiance at each wavelength, again neglecting atmospheric effects (which, as discussed above are wavelength dependent but of second order compared to the cloud effects), can be approximated as a weighted average of the emitted radiance from the cloud and the background surface below the cloud:

$$I_{obs} = \tau \ B(T_{sfc}) + (1-\tau) \ B(T_{cld})$$

<div align="right">Eq. 3</div>

Due to the nonlinearity of the Planck function between the MWIR and LWIR, the resulting brightness temperature computed at each channel for the same cloud and background temperature will increase with decreasing wavelength. This is caused by differences in the relative contributions of the two terms in Eq. 3 at each wavelength. For example, for a transmissive cirrus cloud with a transmissivity of 0.5 at 230 K over a uniform background surface of 280 K, Figure 4 illustrates the relative wavelength dependence of the warm and cold surfaces to the overall radiance. Note in the figure that at 3.9 μm the relative contribution (i.e., the magnitude of the warm surface radiance compared to the cloud surface radiance) from the warm surface is greater than at either 10.8 or 12.0 μm.
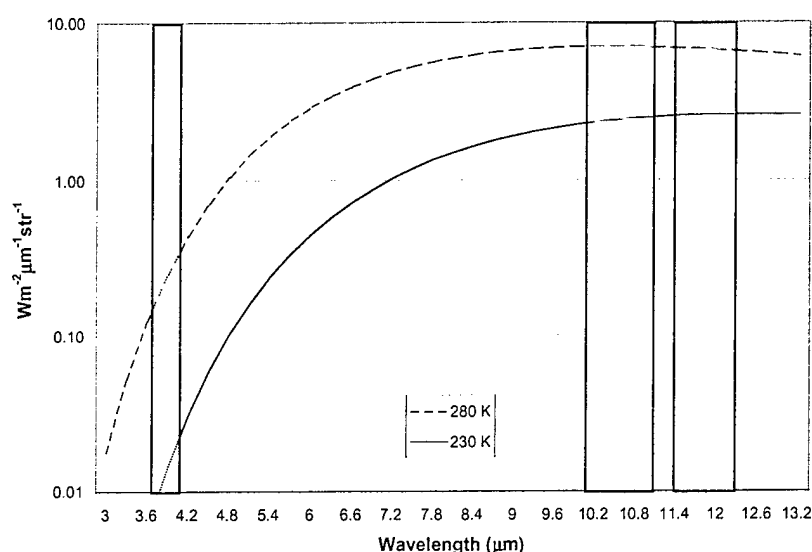
Figure 4 Wavelength dependence of the Planck function for two surfaces at 230 and 280 K, respectively

The magnitude of this difference can be easily calculated by using the radiance values at 3.9 and 10.8 μm and solving Eq. 3 to approximate the TOA radiance that would be measured by an overhead satellite. The resulting brightness temperature can then be computed at each wavelength to illustrate the magnitude of the spectral signature this scene would generate (Table 5). Thus in this example an easily identifiable 8 K spectral signature $(T_{3.9} - T_{10.8})$ would result from the brightness temperatures measured at 3.9 and 10.8 μm. Note that a similar signature would be obtained if the 12.0 channel were substituted for the 10.8.

9

Table 5 **Relative contributions to TOA radiance by a transmissive cloud (τ=0.5) at 230 K and an underlying warm surface at 280 K at 3.9, 10.8 and 12.0 µm**

Wavelength (µm)	Planck Radiance (Wm^{-2}µm^{-1}str^{-1})			Relative Contribution (%)		Brightness Temperature
	Cloud	Surface	TOA (Eq. 3)	Cloud	Surface	
3.9	0.25	0.01	0.13	4	96	267
10.8	7.02	2.48	4.75	26	74	259
12.0	6.70	2.62	4.66	28	72	259

2.2.4 Water Vapor Channel

At 6.7 µm, strong water vapor absorption insures that for all but the driest atmospheres the channel weighting function will peak above the Earth surface (Figure 5). As the total column water vapor increases, or as the distribution of water vapor in the atmosphere moves upward, the radiating temperature measured at 6.7 µm becomes representative of the air higher in the atmosphere. For mid-latitude and tropical regions this results in a strong negative clear-scene brightness temperature differences between 6.7 – 10.8 µm (10.8 selected for comparison as the cleanest window channel). In very dry polar regions the 6.7 µm channel brightness temperature can be representative of the air temperature just above the boundary layer. In situations of strong temperature inversions this can result in a positive 6.7 – 10.8 µm temperature difference.

Figure 5 **6.7 µm weighting function compared to 10.8 µm window channel**

When cirrus optical depth is sufficiently small, transmission of background radiation through the cloud can reduce the cloud-background contrast to a level that cannot be detected by automated cloud algorithms. This can occur in visible, MWIR, and LWIR

10

image bands, and is particularly severe over bright and warm backgrounds such as desert. Under such conditions it may be possible to determine the presence of these transmissive cirrus using wavelengths where the atmosphere is opaque. Using available data in the 6.7-μm water-vapor band we developed a technique to improve detection of thin cirrus clouds over background conditions that are stressing to traditional LWIR and visible techniques and to allow first-order cloud phase discrimination.

2.3 Application to Environmental Satellite Sensor Data

This section provides a description of how the spectral signatures described above are applied to data from existing environmental satellites for classification of pixels as either cloudy or cloud-free. Table 1 summarizes the channel wavelengths used by the various algorithms and identifies which channels are available from existing satellites. The cloud detection algorithm consists of a series of tests each designed to identify a unique cloud or background spectral signature as summarized in Table 2. Recall that no single test is assumed to discriminate all cloud and terrestrial backgrounds in a scene, therefore the algorithm operates by performing each test independently and then computing a final cloud/no cloud classification by evaluating the combined results from all applicable tests together. If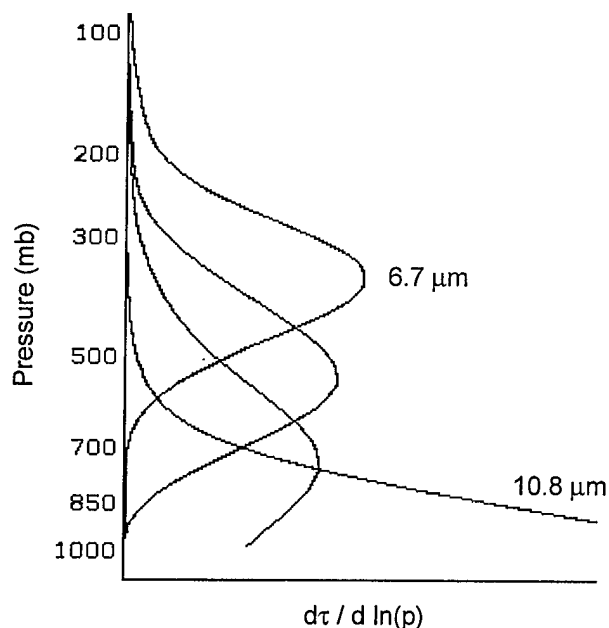 all the sensor channel wavelengths identified in Table 1 are not available for a particular sensor, the algorithm gracefully degrades to execute only those cloud tests for which the required data exist.

2.3.1 Thermally Distinct Cloud Test

The Thermally Distinct Cloud Test is a single LWIR channel threshold test designed to discriminate the thermal signature of obvious mid- and high-level clouds from the terrestrial background signature. From Figure 2 it can be seen that many clouds exhibit a significantly lower brightness temperature than the terrestrial background. Exceptions can occur for highly transmissive cirrus, marine stratus and other low cloud, partially cloud-filled fields of view (FOVs) and high-latitude snow and ice covered backgrounds. Each of these special cases are addressed by other cloud tests described below.

The cloud test requires an estimate of the Earth-surface temperature to predict the IR brightness temperature that the satellite would measure in the absence of cloud. This is predicted by using the best available estimate of the shelter or skin temperature over the region of interest. Generally this comes from an NWP or land- ice- or sea-surface temperature model. For the Contrail support program described in Section 4, we used NWP data from the National Centers for Environmental Prediction (NCEP) ETA and AVN models and radiosonde measurements made during the field programs. The cloud test requires that the LWIR brightness temperature at 10.8 or 12.0 μm be less than the predicted clear-scene temperature by an amount greater than the uncertainty in the clear-scene estimate. Since this test is designed only to detect clouds that exhibit relatively large temperature contrast with the background, no correction is made to the computed satellite-derived EBBT for atmospheric transmission. The magnitude of the threshold is determined by accumulating statistics on the measured difference between satellite EBBTs and the skin or shelter temperature of pixels determined to be cloud-free by previous runs of the cloud algorithm. These statistics are held in a rotating 10-day database stratified by satellite overpass time (i.e., ascending or descending), location, and background geography type.

11

2.3.2 Single Channel Reflectance Test

A VIS to NIR threshold test is used to discriminate relatively high cloud reflectance from a predicted background value. Similar to the Thermal threshold test described above, Figure 2 shows that in the VIS to NIR clouds generally have a greater reflectance than terrestrial backgrounds. Again there are exceptions including transmissive cirrus and certain reflective backgrounds including snow/ice, desert or other high-albedo ecosystems, and sun glint over water surfaces. Each of these special cases are addressed by other cloud tests described below.

If the satellite measured reflectance exceeds the predicted clear-scene background value by an amount greater than an empirically defined threshold, then the pixel is classified as cloud-filled. To maximize cloud contrast with the background, visible-channel sensor data are compared to the predicted while over land surfaces while over water NIR data are used. Separate thresholds are maintained for land and water backgrounds. The test is only applied in the absence of sun glint, desert, or snow/ice covered background conditions.

2.3.3 Near-IR / Visible Reflectance Ratio Test

The Ratio Test compares the relative magnitudes of near-IR 0.86 μm and visible 0.65 μm reflectance values using a channel ratio method. The test makes use of the fact that for most optically thick cloud, the spectral signature in the visible and near IR are very close to each other, while for land and water surfaces they can differ significantly (Figure 2). The test is applied by computing the ratio of the near IR to visible reflectance. No normalization for solar illumination or anisotropic effects are needed since they cancel in the ratio operation. Vegetated land surfaces tend to have a ratio greater than 1.0 due to enhanced reflection in the near IR, and water surfaces less than 1.0 due to greater aerosol and haze scattering in the visible. However, clouds mask the terrestrial signatures resulting in a channel ratio approximately equal to 1.0. Thus, the test for cloud-filled pixels is applied by testing the NIR / VIS ratio against upper and lower cloud threshold values. If the channel ratio falls within these limits then the data are classified as cloud-filled.

Empirical tests have also shown that using a single set of thresholds for all conditions can result in the over analysis of cloud in regions of high humidity. High atmospheric water vapor content is associated with increased concentrations of aerosols and haze, resulting in a preferential increase in atmospheric scattering at visible wavelengths relative to the near-IR. This increased scattering results in a higher measured visible reflectance relative to the NIR for cloud-free areas which can produce a false cloud signature. To account for this the value of the upper and lower thresholds are decreased to account for lower clear-scene channel ratio values.

When making a final cloud decision, the results of the Ratio Test are only used in the absence of sun glint, desert, or snow/ice covered background conditions. All of these conditions tend to eliminate the spectral reflectance differences between land and water surfaces potentially producing false cloud signatures. Similarly the test is not applied over mixed geography types (e.g., coastline) since empirical studies have shown that local variations in background reflectance can be misinterpreted as cloud.

2.3.4 Low Cloud and Fog Test

Low water droplet clouds and fog tend to be thermally indistinct from the background in the LWIR but exhibit high contrast in the VIS to NIR in daytime. As discussed in Section 2.2.3 they also have recognizable spectral signatures in the MWIR when contrasted to LWIR brightness temperatures. In Section 2.2.2 we noted that cloud reflection is negligible at 10.8 and 12.0 μm so that the resulting brightness temperatures are more representative of the true cloud temperature than at 3.9 μm. To supplement the VIS and NIR tests during daytime, and to address the inherent limitation of the Thermal Contrast test to discriminate thermally indistinct cloud at night, the Low Cloud and Fog Test was developed to exploit the MWIR/LWIR signatures. Table 3 and Table 4 illustrate the magnitude of MWIR – LWIR (true cloud) spectral differences for small water droplet clouds that can be expected during day and nighttime, respectively. The sign of the signature changes from day to night from a positive to a negative difference. Also the tables illustrate that the magnitude of signal is larger during daytime due to the relative strength of the reflected solar compared to the weak emission signal. The magnitudes of the thresholds were first established theoretically using Eq. 1 and 2, and then tuned empirically as a function of background surface type using available metsat data. Because of the high reflectance at 3.9 μm of desert and sun-glint, separate thresholds are maintained for desert, non-desert and potential sun glint backgrounds. At night desert surfaces tend to have a lower emissivity at 3.9 μm than other terrestrial surfaces so that separate nighttime cloud detection thresholds are maintained for areas identified as desert by the geography database

2.3.5 Cirrus Cloud Tests

Cirrus clouds pose some of the greatest challenges for automated cloud classification. While optically thick cirrus are generally easily identified through simple thermal contrast with the background, Wylie et al. (1994) documented that cirrus cloud with non-zero transmittance are common throughout the world (Table 6). This results in LWIR brightness temperatures that can be much greater than the true cloud temperature, potentially causing thin high-level cirrus to be misclassified as mid-level cloud. As discussed in Sections 2.2.2 and 2.2.3 cirrus radiative properties in multispectral MWIR to LWIR data support development of algorithms to detect and correctly classify optically thin cirrus. Three separate tests have been developed specifically for this problem.

Table 6 Percentage of global observations containing clouds in various optical depth and pressure categories (Wylie et al., 1994)

Pressure Level [mb]	Visible Optical Depth				
	< 0.3	0.3 – 0.7	0.7 – 1.4	1.4 – 3.0	> 3.0
< 200	1.2	0.4	0.3	0.7	0.9
200 – 300	2.3	1.9	1.6	2.1	1.7
300 – 400	2.5	2.3	2.2	2.4	1.4
400 – 500	2.3	2.5	2.6	2.5	1.1
500 – 600	1.4	2.2	2.5	0.7	1.4
600 – 700	0.6	1.2	1.7	0.7	3.6
700 – 800	0.2	0.4	0.4	0.0	6.6
800 – 900	0.0	0.0	0.0	0.0	11.5
900 – 1000	0.0	0.0	0.0	0.0	6.8

2.3.5.1   LWIR Cirrus Test

The Cirrus Cloud Test examines LWIR window brightness temperature differences between 8.55, 10.8 and 12.0 μm channels to exploit cirrus cloud signatures in this spectral region. As discussed in Section 2.2.2 there are three radiative effects that combine to account for the LWIR cirrus signatures. First, ice particle absorption increases with wavelength across this spectral region. Second, atmospheric water vapor attenuation is slightly stronger at the longer 12 μm wavelengths. Third, there is a slightly stronger Planck dependence on temperature at the shorter wavelengths resulting in a higher relative brightness temperature for what are essentially mixed fields of view that occur with transmissive cirrus. Each of these factors contribute to cirrus brightness temperatures that decrease with wavelength. However, in the absence of cloud, water vapor attenuation can, by itself, cause a positive 10.8 – 12.0 brightness temperature difference that could be mistaken for a cloud signature. Thus, when using a split-LWIR technique to detect cirrus it is necessary to first eliminate cases where the channel difference is caused by clear-scene atmospheric moisture. To accomplish this, the cloud detection threshold is defined as a function of atmospheric water vapor (precipitable water) and path length through the atmosphere.

Real-data tests using the MODIS Airborne Simulator (MAS) and AVHRR measurements demonstrated that the LWIR cirrus signatures are consistent for the majority of climatological situations. However, the test sometimes had difficulty discriminating cirrus cloud from snow and ice backgrounds. To compensate for this, an additional requirement was placed on the cloud test when the background is classified as snow- or ice-covered by external data. Based on the assumption that the 10.8 μm brightness temperature measured from cirrus clouds are colder than the terrestrial background, the 10.8 μm brightness temperature is required to be lower than the predicted clear-scene brightness temperature by an amount greater than a defined cloud detection threshold value.

2.3.5.2 NIR Thin Cirrus Test

Studies using simulated reflectance data in the 1.38 μm water vapor absorption region have shown that detection of very thin cirrus cloud with visible optical depths less than 0.1 is feasible during daytime for most background and scattering angle conditions that will be encountered by MODIS. As discussed in Section 2.2.1, low-level (below cirrus altitudes) water vapor absorption at 1.38 μm effectively masks out reflected solar from the surface beneath the cloud so that, although the cirrus reflectance is not great (typically less than 0.1 for thin cirrus), the contrast with the background is sufficient to detect the cloud. Problematic conditions occur over reflective surfaces with high terrain relief (e.g., snow-covered mountains) and in locations with very low atmospheric water vapor and reflective surfaces (e.g., polar regions).

2.3.5.3 MWIR – LWIR Cirrus Test

Section 2.2.3 describes the basis for transmissive cirrus cloud signatures in the MWIR-LWIR bands in terms of Planck function nonlinearity. Figure 6 shows the magnitude of the cirrus cloud signature as a function of cloud transmittance for a situation where the cloud temperature is 230 K and the underlying surface at 280 K. The ice-cloud signature exists independent of solar illumination, however, a similar signature exists for small water droplet clouds only during daytime (see Section 2.3.4). Additional tests, described below, are required to determine cloud phase.

Normally, the 12.0 μm channel is used for comparison with the 3.9 μm channel in this test. This slightly increases the cirrus cloud signature over that found with the 10.8 μm channel due to the increase absorption by ice particles at the longer wavelength. Note that in Figure 6 there is essentially no difference between the observed temperatures in the 10.8 and 12.0 μm bands emphasizing that the cloud signature is only marginally greater for the 3.9 – 12.0 μm bands relative to the 3.9 – 10.8 μm bands. However, empirical investigation has found that in regions of high humidity the test can over-analyze cloud when using the 12.0 μm band. It is conjectured that when there is no cloud present, water vapor near the surface preferentially absorbs the emitted 12 μm radiation relative to 10.8 μm. As a result when there is sufficient water vapor loading, the derived 12.0 μm EBBT for clear background surfaces can appear sufficiently lower than the true temperature to produce a false detection of cloud. In cases where the integrated water vapor is greater than a defined threshold value then the 10.8 μm data are used in favor of the 12.0 μm channel. The lower sensitivity to water vapor attenuation at the shorter wavelength improves the performance of the cloud test.
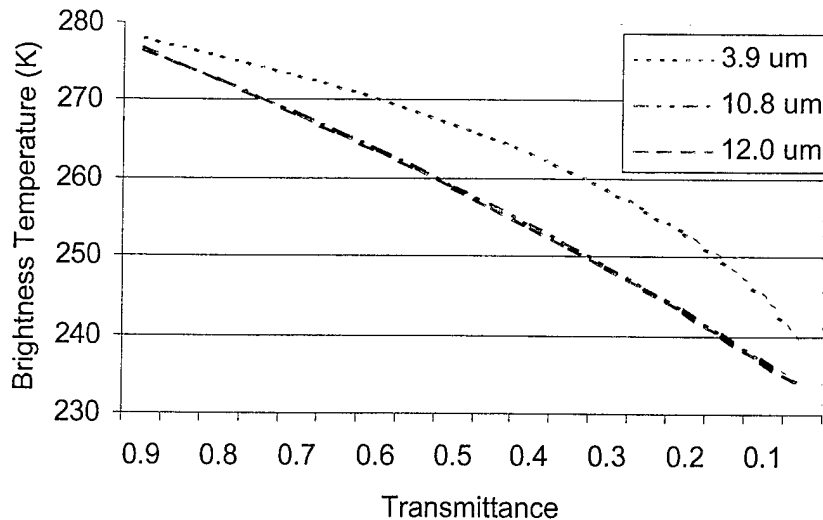
Figure 6 3.9, 10.8 and 12.0 μm brightness temperature dependence on cirrus transmittance. Cloud at 230 K and background at 280 K

2.3.5.4   Water Vapor Channel Cirrus Test

Water vapor imaging channels near 6.7 μm are available on most geostationary satellites and on IR sounders on the NOAA polar platforms. At these wavelengths the sensors measure upwelling thermal radiation emitted primarily by the water vapor in the atmosphere, with little or no contribution from the underlying terrestrial surface. Under cloud-free conditions, the absolute magnitude of a 6.7 μm brightness temperature is dependent on the amount of water vapor that is present along the atmospheric path. Except under conditions of very dry atmospheres, clear-scene brightness temperatures measured at 6.7 μm will be less than temperatures computed for the same scene at LWIR window channel wavelengths. Any cloud in a satellite field of view will reduce the difference between the 6.7 and 10.8 μm brightness temperatures since the 10.8 value will be representative of the ambient temperature at the level of the cloud.

An automated cloud test was developed to exploit this signature. The test evaluates the 6.7 − 10.8 temperature difference for known clear-scene areas and then searches the scene for locations where the difference falls below a cutoff based on the clear-scene difference. While this approach is identical in form to standard single-channel threshold cloud tests, it effectively eliminates dependence on *a priori* knowledge of the surface contributions that can act to mask transmissive cloud signatures. Since knowledge of the surface characteristics is difficult to obtain universally, and is recognized as a significant limitation of other algorithms, this is a potentially major benefit. Sensitivity of the new cloud test was evaluated using nighttime cases where the standard 3.9-10.7 μm multispectral test performs well for detection of thin cirrus. Figure 7 illustrates results obtained for the two techniques applied to a common data set.

(a)   (b)
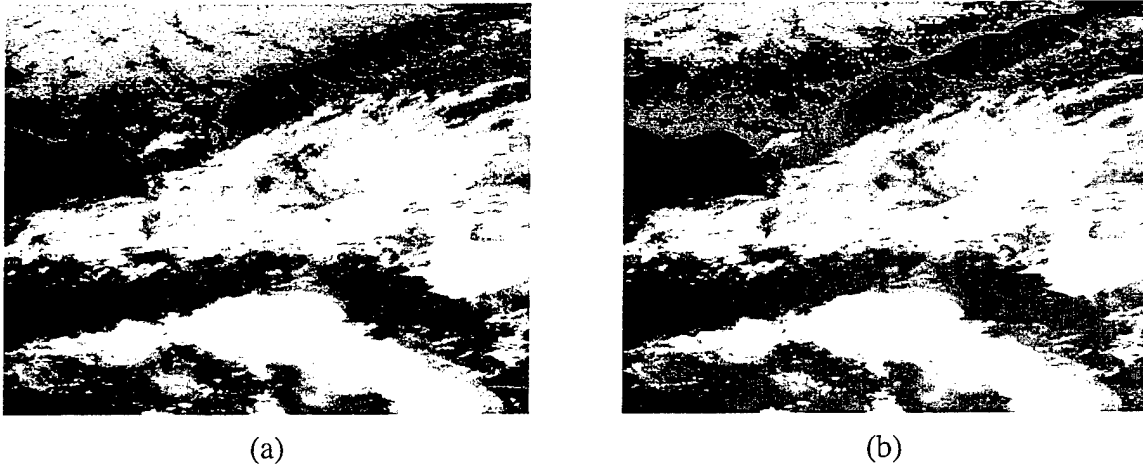
Figure 7 Nighttime detection of thin cirrus using 3.9-10.8 μm multispectral test (a) compared to 6.7-10.8 μm technique (b)

2.3.6 Precipitating Cloud Test

The Precipitating Cloud Test is predominantly a convective cloud test that exploits the reflective nature of vertically-developed clouds at 3.9 μm. As is the case for small water droplet clouds, deep convection type cloud exhibit a 3.9 μm brightness temperature significantly greater than the true physical temperature of the cloud. Since the physical cloud temperature is more accurately represented by the LWIR brightness temperature, the MWIR - LWIR brightness temperature difference is large for this type of cloud. The cloud test requires that the MWIR - LWIR brightness temperature difference exceed a defined threshold value.

A high MWIR - LWIR brightness temperature difference is not in itself uniquely indicative of high, cold, precipitating clouds since small water droplet clouds produce a similar signature for essentially the same reasons. Thus, two other checks are required to discriminate convective cloud from lower liquid water clouds. The first compares the difference in the LWIR brightness temperature from the predicted clear-scene brightness temperature in order to eliminate any low clouds. This check ensures that the true physical cloud top temperature is significantly lower than the predicted clear-scene brightness temperature by comparing the difference to a defined threshold value. The second check requires the near-IR channel reflectance to exceed a defined threshold to eliminate ice clouds that are not as optically thick, and hence not as reflective, as precipitating clouds. This check discriminates between cirrostratus (which generally do not pass this test) and cumulonimbus.

2.3.7 Cloud Phase Classification

Classification of cloud phase (liquid/ice) is required to accurately retrieve the cloud optical and microphysical properties. These are needed for the second part of the Cloud Cover/Layer EDR algorithms to vertically stratify the cloudy pixels into layers. Several

17

of the cloud tests described above use spectral signatures that can be representative of either ice or water cloud (i.e., thermal contrast, precipitating cloud, reflectance tests, daytime MWIR-LWIR cirrus tests).

The phase tests uses spectral signatures representative of ice-phase cloud to classify pixels that are identified as cloudy by any of the preceding tests. Pixels not classified as ice cloud in this way are assumed to be water-phase clouds. The test first checks for LWIR brightness temperatures unequivocally associated with ice cloud (i.e., cloud LWIR temperature < 233 K). At nighttime a positive MWIR-LWIR difference is uniquely found for transmissive cirrus. During daytime, if the NIR (1.38 μm) thin cirrus test detects cloud and none of the other reflectance tests do, then the pixel is assumed to contain transmissive ice cloud. Finally, due to the nearly uniform increase in ice particle absorption with wavelength in the LWIR, coupled with the preferential increase between 10.8 and 12.0 μm for water droplets, an 8.55 – 10.8 μm brightness temperature difference greater than a 10.8 – 12.0 μm difference is indicative of ice cloud while the inverse relationship indicates liquid water cloud.

2.3.8 Sun Glint Test

A sun glint background test is used to detect specular reflection off water surfaces which could be mistakenly identified as cloud by tests that measure reflected solar radiation. The processing logic in these cloud tests require information on the location of specular reflection in order to modify or exclude the tests from the cloud detection process. Specular reflection occurs when the angle of incidence of sunlight equals the angle of reflection and the viewed point lies along a line connecting the solar and satellite subpoints in a plane normal to the viewed point. Thus in general its occurrence is constrained by the geometrical relationships between the sun, satellite and the viewed point. Theory predicts a single specular point for an isotropic surface. This point describes a ray on a satellite image as the satellite and sun move in their respective orbits. However, in practice open water surfaces rarely exhibit isotropic behavior. Wind and wave action increase surface roughness such that the specular geometry is satisfied over large areas of the water surfaces (i.e., on the front, back and sides of wave crests and troughs). The geometric relationships that can be computed from the satellite ephemeris, satellite and solar zenith and sun satellite relative azimuth angles (Figure 8), can only be used to grossly identify regions of possible glint. Models of ocean surface bidirectional reflectance distribution functions exist that can potentially be used to better define glint regions, however they require estimates of wind speed and direction that are not readily available to the cloud cover algorithm. Consequently, spectral tests are used to discriminate cloud from glint.

18
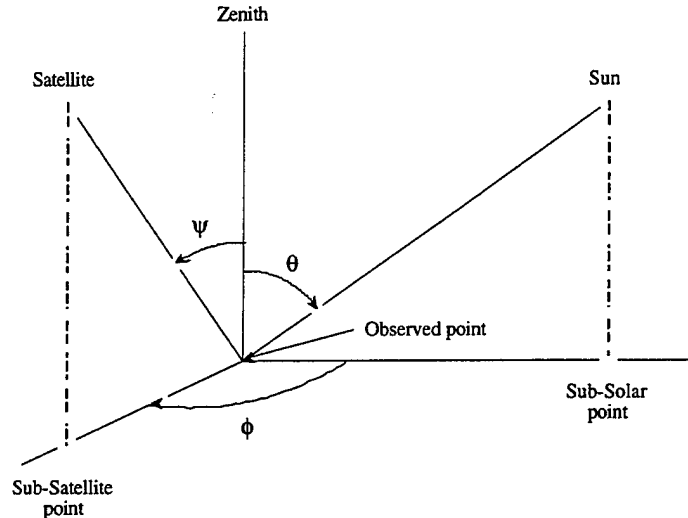
Figure 8 Geometric relationships of sun, satellite and observed point on Earth: ψ - satellite zenith angle; θ - solar zenith angle; φ - relative sun-satellite azimuth angle

The basis for spectral tests to discriminate glint from cloud are the respective reflectance and emission signatures across the spectrum. The approach is to first, identify spectral signatures that are common to both and then, check for signatures that are not representative of cloud. The relevant characteristics in the visible and NIR bands are that both glint and cloud reflectance exhibit little wavelength dependence in this spectral region. However, in the absence of glint cloud-free scenes tend to exhibit a VIS reflectance over open water that is slightly greater than in the NIR due to greater scattering from the small marine aerosol and haze particles at the shorter wavelength. Thus the common cloud and glint reflectance signature is no wavelength dependence across the visible to NIR. Similarly, measured LWIR window channel brightness temperatures for glint, marine stratus, low cloud, or partially cloud filled FOVs will all tend to be close to independent estimates of the cloud-free skin temperature.

Once a pixel is identified as containing either glint or low cloud, additional spectral signatures are examined to perform the discrimination. Mid or high level cloud, including transmissive cirrus, will have an identifiable LWIR thermal contrast with the background. Low level clouds, particularly marine stratus and fog, are generally composed of small water droplets resulting in a computed brightness temperature in the MWIR that is greater than in the LWIR (Section 2.2.3). Glint exhibits a similar signature but with a magnitude that exceeds the level theoretically predicted for cloud with reasonable drop sizes. Also, glint regions do not have a recognizable signature in the longer (emitting) infrared bands. Thus positive results for any of the LWIR cloud tests is treated as an indication that the signal is cloud and not glint.

If the Sun Glint Background Test is positive, then reflectance data from VIIRS Channels below 4.0 μm are considered contaminated and cloud tests that use these data are either not applied or are modified. If the Sun Glint Test cannot be applied due to missing sensor channels, it reverts to a simple geometric test.

19

2.3.9 Desert Background Test

The Desert Background Test is used to discriminate clear-scene desert backgrounds from reflective cloud through the examination of daytime multispectral sensor data. In this application, the term desert is used to indicate any reflective, non-vegetated surface; it does not necessarily follow the geographer's definition of desert based on annual precipitation. Results of this dynamic desert test are used to augment desert information contained in the geography database.

A series of five spectral conditions must be met to classify a pixel as a cloud-free desert background. The first is a modified version of the NIR/VIS Ratio Test. The thresholds used in the test are more limiting than the cloud detection thresholds used in the cloud test since desert land surfaces generally do not exhibit as much variability as clouds in NIR and visible channel measurements. The second test is an absolute check on the NIR reflectance to ensure that the measured value is not large enough to be a cloud signature since desert surfaces are generally not as bright as cloud at that wavelength. The third test checks to determine if the 3.9 μm brightness temperature exceeds a value theoretically predicted as the limit for small water droplet cloud. Clear non-vegetated surfaces can have 3.9 μm reflectance as high as 0.35. The fourth test is used to check the 10.8 μm brightness temperature against the ambient air temperature. The ambient air temperature is determined using the best available estimate of the clear-scene shelter temperature (i.e., temperature of the air 2 m above ground level). This can be obtained from an NWP model, a surface temperature model, or through interpolation of an upper air temperature profile to the actual terrain height at the pixel location. The assumption is that, over desert, a satellite observed solar-illuminated clear-column thermal IR brightness temperature will be close to or exceed the ambient air temperature. The final desert criterion requires that the brightness temperature difference between the 3.9 and 10.8 μm channels be within a specified range. This is to ensure that low clouds are not classified falsely as desert. All five of the above tests must pass in order for a pixel to be considered clear desert background.

2.3.10 Snow/Ice Cover Background Test

Spectral information from multispectral data are used to supplement and update external snow and ice databases. The snow/ice cover background test is used to discriminate snow and ice backgrounds from reflective cloud features using daytime data. The test uses visible and infrared channel data to first identify pixels with characteristics consistent with snow, but not necessarily separate from cloud. A multispectral discriminant is then used to separate snow from cloud. The key spectral signature is the difference in reflectance of snow/ice in the visible and SWIR. Generally snow surfaces reflect well at visible to NIR wavelengths, have low reflectance at 1.6 and 3.9 μm, and have a LWIR brightness temperature close to the expected surface skin temperature. If these collective conditions are met, then the pixel is unambiguously classified as a cloud-free snow/ice surface.

2.4 Cloud Determination

As processing proceeds for each pixel, results of individual cloud tests are stored in a bit-packed data structure called a Cloud Data Record (CDR). Table 7 describes the CDR structure. A final cloud/no-cloud determination is made for each pixel through an evaluation of the individual test results stored in the CDR. While the cloud tests are designed to primarily detect one type of cloud or background, they are not mutually exclusive. More than one cloud test can exhibit a positive result for any particular pixel.

The cloud determination process evaluates the cloud test results differently during daytime and nighttime conditions. Day and night are defined by the local solar zenith angle.

Table 7 Cloud data record bit-map structure

Bit	Description	Identifier
1	Cloud detected mask	CDR.detected
2	Thermally Distinct test	CDR.therm
3	Longwave Cirrus test	CDR.LWci
4	Low cloud and fog test (day/night)	CDR.lcf
5	MWIR-LWIR cirrus test (day/night)	CDR.M-Lci
6	NIR cirrus test	CDR.NIRci
7	Vis/NIR ratio test	CDR.ratio
8	Single channel reflectance test	CDR.reflect
9	Water Vapor channel test	CDR.wtrvpr
10	Cloud Phase test	CDR.phase
11	Land / Water	CDR.land_water
12	Sun glint test	CDR.glint
13	Desert background test	CDR.desert
14	Snow or Ice background test	CDR.snow_ice
15	Precipitating cloud detected	CDR.precip
16	spare	

Under nighttime conditions the process is straightforward. If any of the applicable cloud tests designed to operate under non-solar-illuminated conditions detect cloud, the analysis pixel is classified as cloud-filled. These tests are identified in Table 2 and include: Thermally Distinct, Low Cloud and Fog, LWIR Cirrus, MWIR-LWIR Cirrus, Water Vapor cloud tests.

During solar-illuminated conditions, the process for evaluating the individual cloud test results is more complex. The cloud tests executed only during daytime, or that have a different daytime and nighttime spectral signature are: Single Channel Reflectance, NIR/VIS Reflectance Ratio, Low Cloud and Fog, NIR Thin Cirrus, MWIR-LWIR Cirrus, and Precipitating cloud tests. All of these tests have a dependence on reflected solar radiation and thus can be confused by terrestrial backgrounds with reflectance near or exceeding cloud levels. Supporting data from external databases and results of the spectral sun glint, snow/ice cover, and desert tests are used to determine under what conditions results from the daytime tests will be used in the final cloud classification. The cloud analysis algorithm addresses this problem by either not using or modifying affected tests when reflective backgrounds exist.

The procedure for determination of which tests to run and evaluating the individual cloud test results to compute the final cloud/no-cloud classification is described in Table 8.

Table 8 Procedure for evaluating individual cloud tests

Processing Step	Description
LOOP through each pixel	Loop through all grid boxes touched by current transmission

Initialize all CDR elements to 0
 IF SDR contains bad/missing data THEN
   CDR.bad = 1
   CONTINUE at end of loop
 ENDIF
	Initialize all associated Cloud Data Record output structure – one for each pixel.
	
	 Check for bad pixel data

IF GEOG is DESERT THEN
   Initialize CDR.desert to 1
   Set CDR.land_water = 1
 ENDIF
	Initialize all pixels in grid box based on geography
	
	 Set land/water flag to land for desert points

IF GEOG is LAND   THEN
   Set CDR.land_water = 1
   IF   SOLZEN< solzen_threshold_2   THEN
     run **DESERT** test
   ENDIF
 ENDIF
	Set land/water flag to land – note if not desert or land then flag defaults to water (0).
	
	 Spectral Desert test is conditional on land background and day/night test

IF   SNOW_ICE identifies either SNOW or ICE   THEN
   Initialize CDR.snow to 1
 ELSE
   initialize to 0
 ENDIF
	Initialize all pixels in grid box based on SNOW_ICE.

IF SOLZEN< solzen_threshold_2 THEN
   run SNOW test
 ENDIF
	Spectral Snow test is conditional on solzen(2) day/night test

run THERM test	No initialization or external conditionals imposed on Thermally Distinct test
run LWci	No initialization or external conditionals imposed on Longwave Cirrus test
run PHASE	No initialization or external conditions imposed on Cloud Phase test

IF SOLZEN <solzen_thresh_2 OR solzen_3 THEN
 	
    run REFLECT
 	
ENDIF
	Single Channel Reflectance test required for SUN_GINT and conditional on the larger of two solar zenith thresholds

IF SOLZEN < solzen_thresh_2 AND
    GEOG NE COAST THEN
 	
    run RATIO
 	
ENDIF
	NIR/VIS Reflectance Ratio test required for SUN_GLINT and conditional on solar zenith threshold and GEOG not coast.

IF GEOG is WATER AND GEO_GLINT is set THEN
 	
    IF SOLZEN< solzen_thresh_2 THEN
 	
      run **SUN GLINT**
 	
    ELSE IF SOLZEN < solzen_thresh_1 OR
              SOLZEN < solzen_thresh_3 THEN
 	
      CDR.glint = 1
 	
    ENDIF
 	
ENDIF
	SUN_GLINT is conditional on WATER background, GEO_GLINT, and solzen(2) and requires output from COLD, CIRRUS, VIS_B, RATIO.
	
	IF SZE is greater than solzen(2) but less than either (1) or (3) use GEO_GLINT for water backgrounds

IF CDR.glint is set THEN
 	
    CDR.reflect = CDR.ratio = 0
 	
ENDIF
	Reset reflect and ratio test results (previously run for glint test) on a pixel-by-pixel basis for all pixels in 16th cell to exclude glint

IF SOLZEN > solzen_thresh_3 THEN
 	
    CDR.visb = 0
 	
ENDIF
	Reset reflect test results (previously run for glint test) to make test conditional on solzen_thresh_3

IF SOLZEN < solzen_thresh_1 THEN
 	
    run LCF(day)
 	
ELSE
 	
    run LCF(night)
 	
ENDIF
	LCF day/night versions of test conditional on solzen_thresh_1

IF SOLZEN < solzen_thresh_2 THEN
 	
    run PRECIP
 	
    run M-Lci(day)
 	
    run NIRci
 	
ELSE
 	
    run M-Lci
 	
ENDIF
	PRECIP test and MWIR-LWIR and NIR cirrus test
	
	MWIR-LWIR day/night versions of tests conditional on solzen_thresh_2

23

IF CDR.therm OR	Define cloud-detected mask
CDR.LWci OR	All dependencies and conditionals have been applied above – cloud mask is simply logical OR of individual cloud tests.
CDR.lcf OR	
CDR.M-Lci OR	
CDR.NIRci OR	
CDR.ratio OR	
CDR.reflect OR	
CDR.precip THEN	
CDR.detected = 1	
ENDIF	
END LOOP	End of pixel-level processing loop for current grid cell

Input data requirements and data dependencies for each cloud test are summarized in Table 9 and Table 10.

Table 9 Cloud test data requirements and dependencies

Tests → Inputs ↓	Day								Night			Day/Night			
	Glint	Desert	Snow	Ratio	Reflect	Precip	NIRci	LCF	M-Lci	LCF	M-Lci	Therm	LWci	WtrVpr	Phase
Glint				X	X	X		X	X						
Desert				X	X	X		X	X	X		X			
Snow				X	X	X		X	X			X	X		X
Therm	X														
M-Lci	X														
Ratio	X														
Reflect	X														
R 65		X	X	X	X										
R 85		X	X	X	X	X									
R 1.3							X								
R 1.6			X												X
T_3.9	X	X	X			X		X	X	X	X				X
T 6.7														X	
T 8.5													X		X
T 10.8	X	X	X			X		X	X	X	X	X	X	X	X
T 12.0									X		X			X	X
Geog	X	X			X	X		X		X		X			
SatZen	X							X						X	
SolZen	X	X	X	X	X	X		X	X	X					X
Az	X							X							
Terrain		X													
Tpred				X	X	X						X	X		X
Apply	water	land	water or land	no snow, glint, desert, coast	no snow, glint, desert	no snow, glint, desert		no snow, glint							

24

Table 10 Key to abbreviations used in Table 9

Abbreviation	Description
Glint	Spectral sun glint test
Desert	Spectral desert test
Snow	Spectral snow test
Therm	Thermally distinct cloud test
Reflect	Single channel reflectance cloud test
Ratio	NIR/VIS reflectance cloud test
LCF	Low cloud and fog test
LWci	LWIR cirrus test
NIRci	NIR cirrus test
M-Lci	MWIR – LWIR cirrus test
Precip	Precipitating cloud test
WtrVpr	Water vapor channel cloud test
Phase	Cloud phase classification test
R_65	0.65 μm reflectance
R_85	0.85 μm reflectance
R_1.3	1.3 μm reflectance
R_1.6	1.6 μm reflectance
T_3.9	3.9 μm brightness temperature
T_6.7	6.7 μm brightness temperature
T_8.5	8.5 μm brightness temperature
T_10.8	10.8 μm brightness temperature
T_12.0	12.0 μm brightness temperature
Geog	Geography database containing land, water boundaries and eco-system type
SatZen	Satellite zenith angle (Figure 8)
SolZen	Solar zenith angle (Figure 8)
Az	Relative satellite-solar azimuth angle (Figure 8)
Terrain	Terrain height MSL
Tpred	Predicted clear scene brightness temperature

2.5 External Data Requirements

As discussed above, in addition to the satellite sensor data identified in Table 1, the individual cloud tests require some additional externally-provided supporting data. These data are typically obtained from an NWP model or static database. Table 11 summarizes the supporting data requirements.

25

Table 11 Non-satellite external data requirements

External Data	Usage
Surface temperature analysis or climatology	characterize natural variability of clear-scene thermal IR channel backgrounds and provide first guess to predicted clear-scene temperature algorithm that is part of cloud detection algorithm
NWP boundary-layer temperature analysis or forecast	characterize natural variability of clear-scene thermal IR channel backgrounds and provide first guess to predicted clear-scene temperature algorithm that is part of cloud detection algorithm
NWP or radiosonde upper air analysis or forecast	provide temperature-height profile for use in assigning pixel-level cloud height
Geography database	provide first-order information on land/water/desert boundary locations

2.6 Algorithm Tuning

Each of the cloud tests described above use one or more cutoff thresholds to determine whether a spectral signature is consistent with cloud or a background type. Thresholds can take various forms such as the magnitude of sensor channel brightness temperature differences, reflectance values, zenith angle cutoffs, etc. Tuning is performed to adjust the sensitivity of each test to match end user requirements. Threshold values were empirically adjusted to bring the analysis products into conformity with manual interpretations of imagery generated from the input sensor data.

3. Cloud Property Retrievals

After a cloudy scene has been classified using the cloud detection and phase discrimination algorithm described in Section 2, cloud particle size, emissivity, and physical temperature are estimated for the cirrus pixels. Cirrus property retrievals are performed using a coupled algorithm that simultaneously retrieves these cloud attributes using radiances measured in the mid-wave infrared (MWIR), water-vapor (WV), and thermal infrared (TIR), nominally at 3.9, 6.7, 10.8, and 12.0 μm. From a radiative-transfer point of view cirrus emissivity, effective particle size, and effective temperature (defined here as the temperature of the radiative "center of mass" of the cirrus cloud) are interdependent. For this reason all three cloud attributes are estimated simultaneously using a first-principles algorithm that numerically solves a set of simultaneous radiance equations. Cloud optical thickness is also estimated at visible wavelengths. Cloud-top height and pressure are diagnosed subsequently via coincident atmospheric temperature profiles.

The cirrus retrieval algorithm uses a simultaneous-solution approach to ensure physical consistency between satellite radiance measurements and theoretical radiative transfer calculations. The fundamental non-uniqueness of the relationship between measured radiance and cloud emissivity, particle size, and temperature at a single wavelength is resolved by forcing the retrieved parameters to be simultaneously consistent with theory and satellite observations at multiple infrared wavelengths.

Preliminary comparison of this approach with ground-based radar observations shows a good match, confirming the potential of our radiative transfer modeling strategy and overall multispectral paradigm.

3.1 Cirrus Attributes

This section summarizes the cirrus attributes that are retrieved using our algorithm. For emissivity, particle size, and cloud-top temperature our approach is to retrieve these parameters simultaneously, since from a radiative point of view they are not independent of one another. Our radiative-transfer theory also requires as a by-product the specification of other cirrus microphysical and radiative attributes such as ice-water path and optical thickness.

Cirrus effective particle size is defined as the ratio of the third moment of the ice-crystal size distribution to the second moment, averaged over a layer of air within a cloud. Cirrus optical thickness is the extinction (scattering plus absorption) vertical optical thickness of the cloud. Optical thickness τ is related to the transmittance t by the relation

$$t = e^{-\tau}. \hspace{4cm} \text{Eq. 4}$$

Effective cloud-top temperature (height, pressure) is valid for the radiative center of mass of the cirrus cloud, "effectively" placing it as an infinitesimally thin slab at a single atmospheric level. Thus the retrieved temperature (height, pressure) is that which, in combination with the retrieved emissivity, yields the same upwelling radiance observations for the theoretically thin slab as does the actual cirrus cloud of some vertical extent.

Cirrus ice-water path is a by-product of our retrieval approach, as will be shown in the next section. It is defined as the vertical summation of the mass of all ice crystals in the cirrus cloud per unit area, and typically has units of g/m^2.

3.2 Cloud Property Algorithm Description

This section describes the scientific basis of the cirrus emissivity, particle size, and cloud effective temperature retrieval algorithm. Our approach is to retrieve these parameters simultaneously, since from a radiative point of view they are co-dependent on one another. Cloud effective temperature can be thought of as the temperature at the cloud's radiative "center of mass," and does not usually correspond to the physical top of the cirrus cloud unless it is optically very thick. However the retrieved cloud effective temperature is a marked improvement over temperatures that are computed using a blackbody assumption, especially for transmissive cirrus. It may be possible to retrieve with some skill the actual cirrus cloud top and cloud base using relative humidity profiles that are coincident with the satellite-based report of cloud, but this is not a part of this study.

3.2.1 The Cloud Retrieval Problem

Clouds exist globally throughout the troposphere. Their effects on remotely sensed top-of-atmosphere (TOA) radiances emitted at thermal infrared wavelengths are highly variable both temporally and spatially.

The only tractable theory for describing the radiative properties of clouds is the electromagnetic theory for scattering of light by spheres (Mie theory). Scattering of light by spherical water droplets is largely a solved problem. Given a spherical particle of radius r and complex refractive index

$$n = n_{re} + in_{im},$$
<div align="right">Eq. 5</div>

where n_{re} the real part accounts for scattering and n_{im} the imaginary part and accounts for absorption within the particle, Mie theory provides the means for computing the extinction efficiency factor Q_{ext}, the scattering efficiency Q_{sca}, and the phase function $P(\Theta)$ for a given scattering angle Θ. Other relevant properties, such as the single-scattering albedo ω and asymmetry parameter g, can be derived from the above quantities. All parameters derived from Mie calculations are wavelength-dependent.

Scattering by non-spherical ice crystals is substantively more problematic due to the non-uniform shape of the scatterer. While much progress has been made in this area, significant uncertainties remain, such as the phase function and its dependence on environmental conditions (e.g., crystal shape and its dependence on temperature).

The net radiative effects of an atmospheric cloud layer depend on its size distribution n(r), which is the number of particles per unit volume per particle-size radius increment: common units for n(r) are $cm^{-3} \mu m^{-1}$. Bulk radiative attributes of the entire cloud layer are computed as a frequency-of-occurrence weighted sum of the Mie-computed variables for a set of cloud particle radii. For example, the extinction coefficient β_{ext} for cloud layer is given by

$$\beta_{ext} = \int_0^\infty \pi r^2 Q_{ext}(r, \lambda, m) n(r) dr .$$
<div align="right">Eq. 6</div>

The radiative effects of a cloud layer depend strongly on its particle size distribution. Many size-distribution shapes are used in radiative transfer models for cloudy atmospheres, but the most common are a modified gamma distribution for spherical water droplets (e.g., Miles et al., 2000) and a bimodal gamma distribution for non-spherical ice crystals (e.g., Mitchell et al., 1996). Gamma distributions are reasonably consistent with in-situ observations of cloud particles, although variations on these shapes occur that are functions of cloud formation processes (e.g., convective or stratiform). The vertical distribution of ice-cloud particle sizes also tends to vary with temperature.

Knowledge of the cloud droplet (crystal) size distribution, refractive index, total liquid (ice) water path, and vertical distribution of mass within the cloud is required to properly parameterize radiative transfer models. Calculation of top-of-atmosphere infrared radiances requires consideration of cloud scattering and absorption, multiple-scattering interactions between cloud particles and atmospheric gases, and absorption by atmospheric water vapor.

3.2.2 Ice Crystal Emissivity and Temperature

Analytic approximations to full geometric-scattering theory for nonspherical ice-crystals have been developed for use in simulating thermal infrared (TIR) bands. This section describes the theory and summarizes its application in our retrieval process.

The infrared upwelling radiance $I_{\lambda,TOA}$ at wavelength λ in a non-scattering atmosphere and for a cirrus-filled pixel is well approximated by

$$I_{\lambda,TOA} = (1 - \varepsilon_\lambda) I_{\lambda,clr} + \varepsilon_\lambda B_\lambda(T_{cld}), \qquad \text{Eq. 7}$$

where ε_λ is the cirrus emissivity at wavelength λ; $I_{\lambda,clr}$ is the TOA radiance that would be observed in an otherwise cloud-free pixel; and $B_\lambda(T_{cld})$ is the cirrus Planck blackbody radiance, a function of the cirrus effective emitting temperature T_{cld}.

As an aside, the overall retrieval paradigm is to write Eq. 7 for two wavelengths and solve them simultaneously using an iterative numerical approach. At first glance, Eq. 7 has two unknowns in emissivity ε and cirrus temperature T_{cld}, making such a solution possible in a strictly mathematical sense. In practice, the improper choice of the two wavelengths can make the solution unstable and poorly defined. These issues are all discussed in later sections, but the overall approach is mentioned here to keep in mind as the theoretical discussion of our radiation transfer model continues.

Effective temperature is understood in its proper context via Eq. 7: T_{cld} is not the cloud-top temperature, but rather the temperature of the radiative "center of mass" of the cirrus cloud. This is evidenced by the fact that the second term on the right side of Eq. (2) represents the integration of layer radiances over the entire depth of the cirrus. Mathematically, ε_λ and T_{cld} are the values that make the expression

$$\varepsilon_\lambda B_\lambda (T_{cld}) = \int_{t_{base}}^{t_{top}} B_\lambda [T_{cld}(t)] dt \qquad \text{Eq. 8}$$

true. In Eq. 8, "t" denotes the transmittance profile of the cirrus cloud, due only to the ice crystals. Atmospheric attenuation within and above the cirrus cloud is formally neglected in the formulation of Eq. 7, but in practice represents a source of error in T_{cld}. However, since water vapor is the primary and relatively weak atmospheric absorbing constituent in TIR window bands, its influence at and above cirrus levels on TOA radiances is minimal.

In general, cirrus effective temperature is not representative of the cirrus cloud top temperature. However, it helps diagnose the wavelength dependence of cirrus emissivity. Additionally, it can be used as a seed into the relative humidity profile to retrieve cloud top and cloud base (this is a subject for future research and was not a part of this study).

Equation 7 forms the basis for the radiative-transfer model in our cloud implementation. Neglecting cirrus reflectivity, absorption optical thickness τ_{abs} is related to cirrus emissivity ε via the expression

$$1 - \varepsilon = e^{-\tau}. \qquad \text{Eq. 9}$$

Thus Eq. 7 can be written

$$I_{\lambda,TOA} = \exp(-\tau_{\lambda,abs}) I_{\lambda,clr} + [1 - \exp(-\tau_{\lambda,abs})] B_\lambda(T_{cld}), \qquad \text{Eq. 10}$$

where $\tau_{\lambda,abs}$ is the cirrus bulk absorption optical thickness at wavelength λ. All that is needed to use Eq. 10 within our simultaneous-equation retrieval framework is a physically consistent model that relates cirrus optical thickness at multiple wavelengths to effective particle size and temperature. This need motivates the development of the geometric scattering theory by non-spherical ice crystals which is outlined next.

3.2.3 Ice Crystal Diameter

Cloud attributes that will be shown to be a by-product of our retrieval approach include effective diameter (D_{eff}) and visible optical depth (τ_{vis}). Each of these is related to ice water path (IWP). First the definition of effective diameter with respect to irregularly shaped ice crystals is addressed.

The concept of an effective distance or photon path, d_e, as being a particle volume-to-area ratio was first suggested by Bryant and Latimer (1969) and further developed in Mitchell and Arnott (1994) and Mitchell et al. (1996) to treat absorption and extinction by ice particles. The last two citations define d_e for ice particles as the volume V (cm^3) defined as bulk ice density divided by the particle's projected area at random orientation, P (cm^2):

$$d_e = m / (\rho_i P),$$

Eq. 11

where m is the particle's mass (g), and bulk ice density $\rho_i = 0.92$ g cm^{-3}. This value of ρ_i must be used since ice refractive indices are referenced to bulk ice density. This concept of d_e is borne out of the anomalous diffraction approximation (ADA), a simplification of Mie theory (van de Hulst 1981). ADA approximates the absorption efficiency as

$$Q_{abs} = 1 - \exp(-4\pi n_i d_e / \lambda),$$

Eq. 12

where n_i is the imaginary part of the refractive index and λ is the wavelength. As defined in Eq. 11, d_e is the representative distance a photon travels through a particle without internal reflections or refraction occurring. In Mitchell (2000), henceforth M00, it is shown that relevant processes not included in ADA can be parameterized into ADA such that this modified ADA yields absorption efficiencies with errors ~10% or less relative to Mie theory. Absorption processes represented in the modified ADA are based on the principle of effective photon path, indicating that d_e is the relevant dimension for single particle-radiation interactions. We can take this a step further, and relate the diameter of a sphere, D, to its effective distance, d_e. Using ice spheres as an example in Eq. 11, mass $m = \rho_i(\pi D^3/6)$ and projected area $P = \pi D^2/4$, give

$$d_e = 2/3 \, D.$$

Eq. 13

If there is an effective photon path for a single particle, it can be asked if there is also an effective photon path for the entire size distribution, N(D). Based on the formalism in Eq. 11, such a photon path should be defined for ice size spectra as

$$D_e = IWC / (\rho_i P_t),$$

Eq. 14

30

where IWC is the cirrus cloud ice water content (g cm^{-3}), and P_t is the total projected area of all ice crystals in the size distribution (with units of area per unit volume cm^2 cm^{-3} = cm^{-1}). Projected area P_t is the geometric cross-sectional area per unit volume of a distribution of ice crystals with random orientations. Based on Eq. 13, the effective diameter of the size distribution should then be 3/2 d_e or

$$D_{eff} = 3\ IWC\ /\ (2\ \rho_i\ P_t)\,, \qquad\qquad \text{Eq. 15}$$

again where IWC is the ice water content of the size distribution.

The same formalism applies to water clouds. That is, the standard definition of effective radius used for water clouds, r_{eff}, is equivalent to Eq. 15. Defining r_{eff} as _ D_{eff}, then

$$r_{eff} = 3\ LWC\ /\ (4\ \rho_w\ P_t)\,, \qquad\qquad \text{Eq. 16}$$

where LWC is the liquid water content (g cm^{-3}), and ρ_w is the density of liquid water (1 g cm^{-3}). The LWC and P_t are defined as

$$LWC = \int \rho_w\ (4/3)\ \pi\ r^3\ N(r)\ dr\,, \qquad\qquad \text{Eq. 17}$$

and

$$P_t = \int \pi r^2\ N(r) dr, \qquad\qquad \text{Eq. 18}$$

where N(r) dr is the size distribution with respect to radius. Substituting Eqs. 17 and 18 into Eq. 16 yields the traditional definition of effective radius, as defined in Slingo (1989):

$$r_{eff} = \frac{\int r^3\ N(r)dr}{\int r^2\ N(r)dr}. \qquad\qquad \text{Eq. 19}$$

This illustrates how there is a single general definition for effective radius or diameter for all clouds, regardless of phase, and that this definition can be understood physically as the representative photon path for all particles in the size distribution.

3.2.4 Absorption of Infrared Radiation by Ice Clouds

The coefficients for absorption and extinction are defined as follows:

$$\beta_{abs} = \int_0^{\infty} Q_{abs}(D,\lambda)P(D)N(D)dD\,, \qquad\qquad \text{Eq. 20}$$

and

$$\beta_{ext} = \int_0^\infty Q_{ext}(D,\lambda)P(D)N(D)dD \qquad \text{Eq. 21}$$

where N(D) is the size distribution and D is particle maximum dimension. If D_{eff} is the appropriate dimension for describing particle-radiation interactions for a size distribution, then it is natural to ask what the consequences might be if the efficiencies Q_{abs} and Q_{ext} were to be taken outside the integrals of Eqs. 20 and 21, and solved for in terms of D_{eff}. This results in the following simple equations

$$\beta_{abs} = Q_{abs}\, P_t \qquad \text{Eq. 22}$$

and

$$\beta_{ext} = Q_{ext}\, P_t\,, \qquad \text{Eq. 23}$$

where Q_{abs} and Q_{ext} are efficiencies representing the entire size distribution. Although β_{ext} has been formulated in terms of D_{eff}, derivations here are restricted to β_{abs} since tests have indicated that emissivities are accurately predicted using the zero scattering approximation, where only β_{abs} is needed. The retrieval methodology that follows is based on thermal infrared emissivities. Expressions for Q_{abs} and P_t are given below. Equation 22 will be tested against Mie theory in the next section.

The gamma size distribution has the form

$$N(D) = N_o\, D^v\, e^{-\Lambda D}\,, \qquad \text{Eq. 24}$$

where N_o is related to the IWC and number concentration N. The gamma distribution N(D) has mean $(v+1)/\Lambda$ and variance $(v+1)/\Lambda^2$. Again, as a reminder, D is the maximum dimension of an ice crystal in a cirrus cloud that has a size distribution of the form given by Eq. 24. The mass- and projected-area dimensional power law expressions for m and P of an individual ice crystal are

$$m = \alpha\, D^\beta \qquad \text{Eq. 25}$$

and

$$P = \sigma\, D^\delta\,, \qquad \text{Eq. 26}$$

where D is the maximum dimension of the ice crystal (cm), P the cross-sectional area (cm^2), and m the mass (g). It is seen that the constants σ, δ, α, and β relate the cross-

sectional area and mass of a single ice crystal to that crystal's maximum dimension. Equations 25 and 26 are obtained by performing a regression analysis of the forms

$$\ln m = \ln \alpha + \beta \ln D \qquad \text{Eq. 27}$$

and

$$\ln P = \ln \sigma + \delta \ln D , \qquad \text{Eq. 28}$$

respectively, for a large variety of crystal shapes and sizes (i.e., maximum dimensions). The constants σ, δ, α, and β are dependent on ice-crystal shape and size, and are determined experimentally using *in-situ* aircraft observations of cirrus ice-crystal shapes, cross-sectional areas, and volumes.

A general expression for the size distribution projected area is given as

$$P_t = \sigma N_o \Gamma (\delta + v + 1) / \Lambda^{\delta + v + 1} \qquad \text{Eq. 29}$$

where D = maximum particle dimension and Γ denotes the gamma function. Expressions 25 and 26 are defined for various ice particle shapes in Mitchell (1996) and Mitchell et al. (1996a, b). The parameters v, Λ, and N_o can be obtained from measurements of the distribution of D properties [N(D)] as described in Mitchell (1991):

$$v = [(\beta + 0.67) \underline{D} - D_m] / (D_m - \underline{D}) , \qquad \text{Eq. 30}$$

$$\Lambda = (v + 1) / \underline{D} , \qquad \text{Eq. 31}$$

and

$$N_o = IWC \ \Lambda^{\beta + v + 1} / [\alpha \ \Gamma(\beta + v + 1)] , \qquad \text{Eq. 32}$$

where $\underline{D}$ is the mean of N(D), and D_m is the maximum particle dimension that divides the N(D) mass into equal parts. Substituting Eq. 14 into 12 but in terms of spheres having the same D_e value (i.e., for $D_e = 2/3 \ D_{eff}$) yields

$$Q_{abs,ADA} = 1 - \exp (-8 \pi n_i D_{eff} / 3 \lambda) , \qquad \text{Eq. 33}$$

where $Q_{abs,ADA}$ is the absorption efficiency representing the entire size distribution based on ADA. When the exponent $-8\pi n_i D_{eff} / 3\lambda$ is "large," absorption efficiencies are dominantly a projected-area-dependent phenomenon. When $-8\pi n_i D_{eff} / 3\lambda$ is "small," absorption efficiencies are dominantly volume-dependent (i.e., ice-mass dependent; Mitchell and Arnott, 1994).

For a general solution for water and ice clouds, the complete expression for Q_{abs} as parameterized in M00 can be used, which includes the processes of (a) absorption due purely to the physical cross-section of a crystal, (b) internal reflection/refraction, and (c) photon "tunneling," which can be thought of as all absorption processes that exclude (a) and (b). Tunneling here is a process by which photons beyond a particle's geometric cross-section would be absorbed if the particle is a blackbody. These processes were also expressed in terms of an "effective photon path," or d_e. Therefore, Q_{abs} may be approximated for all absorption processes in terms of D_{eff}:

$$Q_{abs} = (1 + C_1 + C_2) Q_{abs,ADA} .$$

Eq. 34

The leading term (the "1") on the right side of Eq. 34 represents absorption via the particle's geometric cross section. The term C_1 accounts for absorption contributions from internal reflection and refraction, and the photon tunneling term C_2 in M00 is expressed in terms of D_{eff}, wavelength, and index of refraction.

Equation 22 is then solved using Eq. 27 and Eq. 34. The expression given by Eq. 22, namely

$$\beta_{abs} = Q_{abs} P_t ,$$

has been compared with numerical Mie theory integrations over size distributions of water droplets, and against observations of absorption efficiencies for non-spherical ice crystals. Errors relative to $Q_{abs,Mie}$ are low (generally within 10%), and for small ice crystals grown in a cloud chamber the errors between observation and the modified ADA theory are within 3%.

One of the major output components of our retrieval approach (as defined by simultaneous solution of Eq. 7 at two wavelengths) is the estimated emissivity ϵ at a 10.8-μm TIR channel, corresponding to temperature T_{cld} at the cloud's radiative center of mass. Based on this, the algorithm determines ϵ at all other IR channels, based on the radiation transfer theory described by Eqs. 34, 29, and 22. The theoretical development for emitted terrestrial radiation is described in its most fundamental form by these four equations, and is applied below for the purpose of retrieving IWP. Assuming no scattering at thermal wavelengths,

$$\epsilon = 1 - \exp(-\tau_{abs} / \cos\theta_{sat}) ,$$

Eq. 35

where θ_{sat} is the satellite zenith angle and τ_{abs} is the absorption optical depth. Dividing optical depth by the factor $\cos\theta_{sat}$ accounts for increased path length through the cirrus due to non-nadir views. For a cirrus cloud where the size distribution (SD) is invariant with in-cloud position, the absorption optical depth is given by

$$\tau_{abs} = \beta_{abs} \Delta z ,$$

Eq. 36

where Δz is the cloud physical depth (from top to base) and β_{abs} is the absorption coefficient, defined by Eq. 20 as

$$\beta_{abs} = \int_0^\infty Q_{abs}(D,\lambda)P(D)N(D)dD \qquad \text{Eq. 37}$$

where $Q_{abs}(D,\lambda)$ is the absorption efficiency at wavelength λ for ice crystals of maximum dimension D; P(D) is the projected area for a crystal of maximum dimension D (see Eq. 26), and N(D) is the ice-crystal size distribution (e.g., Eq. 24). D has dimensions of length, P of area, and N(D) of "per unit volume per unit length;" Q_{abs} is dimensionless. It follows that the absorption coefficient β_{abs} has units of inverse length.

From Equations 22 and 34, τ_{abs} is expressed as

$$\tau_{abs} = Q_{abs} P_t \Delta z . \qquad \text{Eq. 38}$$

3.2.5 Ice Water Path

Equation 38 can now be combined to solve for the ice water path IWP (g cm^{-2}), which is the melted-equivalent water mass per unit area of a column through the entire extent of the cirrus cloud. By definition, and assuming that IWC is the vertically averaged value,

$$\text{IWP} = \text{IWC} \, \Delta z \qquad \text{Eq. 39}$$

then Eq. 15 becomes

$$D_{eff} = 3 \, \text{IWP} / (2 \, \rho_i \, P_t \, \Delta z) , \qquad \text{Eq. 40}$$

giving

$$\text{IWP} = 2 \, \rho_i \, D_{eff} \, \tau_{abs} / (3 \, Q_{abs}) . \qquad \text{Eq. 41}$$

Substituting for τ_{abs} and using Eq. 41, Eq. 35 can be rewritten as

$$\varepsilon = 1 - \exp(-3 \, \text{IWP} \, Q_{abs} / 2 \, \rho_i \, D_{eff} \cos \theta_{sat}) . \qquad \text{Eq. 42}$$

Solving Eq. 42 for IWP yields

$$\text{IWP} = -2 \, \rho_i \, D_{eff} \cos \theta_{sat} \ln(1 - \varepsilon) / (3 \, Q_{abs}) . \qquad \text{Eq. 43}$$

Note that D_{eff} appears both in the numerator and in the denominator within Q_{abs} (see Eqs. 33 and 34).

35

Fortunately, we have exploited a means of estimating D_{eff} in tropical anvil and mid-latitude cirrus as a function of cirrus environmental temperature (Mitchell et al., 2000). The tropical scheme is based on 93 measured N(D) from three tropical anvils reported in McFarquhar and Heymsfield (1996) for the CEPEX field campaign, three tropical anvils reported in Knollenburg et al. (1993), and a tropical tropopause cirrus case (Heymsfield 1986). Mid-latitude schemes are based on *in-situ* measurements of cirrus taken during the ARM campaign in the central U.S.

3.2.6 Visible Extinction Optical Depth

Once the absorption optical thickness is computed at a TIR wavelength, it is then transformed into a visible total extinction optical depth $\tau_{ext,vis}$. At visible solar wavelengths, the extinction efficiency, Q_{ext}, is well approximated as 2.00 for ice particles in cirrus. This corresponds to size parameters $\pi d/\lambda \geq 30$. At "visible" wavelengths, say $\lambda = 0.5\ \mu m$, size parameters greater than 30 correspond to effective diameters $d \geq 5\ \mu m$, which is always the case for cirrus ice crystals, even at the tropical tropopause. The visible optical depth can easily be determined beginning with the definition of the extinction coefficient, namely

$$\beta_{ext} = \int_0^\infty Q_{ext}(D,\lambda)P(D)N(D)dD \cong 2P_t \qquad \text{Eq. 44}$$

Recalling the definition of D_{eff} from Eq. 15, and expressing Eq. 15 in terms of the total N(D) projected area per unit volume P_t ($cm^2\ cm^{-3} = cm^{-1}$), substituting P_t into Eq. 44 gives

$$\beta_{ext,vis} = 3\ IWC / (\rho_i\ D_{eff})\ . \qquad \text{Eq. 45}$$

If $\beta_{ext,vis}$ is constant throughout the cloud, then $\tau_{ext,vis} = \beta_{ext,vis}\ \Delta z$. Since $IWP = IWC\ \Delta z$,

$$\tau_{ext,vis} = 3\ IWP / (\rho_i\ D_{eff})\ , \qquad \text{Eq. 46}$$

If we assume zero scattering, then when $\varepsilon = 0.90$, 10% of the radiance at cloud base is transmitted to space. Since we are dealing with conditions where such transmission is generally > 5%, then D_{eff} is derived from radiance from all cloud levels. Due to this, Eq. 46 yields a $\tau_{ext,vis}$ comparable with a $\tau_{ext,vis}$ calculated from *in-situ* measurements of the size distribution.

4. Application to Real Data

With a methodology to compute emissivity as a function of wavelength, effective particle size, and cirrus environmental temperature, it is now possible to solve a simultaneous set of equations as defined by Eq. 7 for two GOES infrared bands using an iterative numerical approach. The clear-scene radiance estimate $I_{\lambda,clr}$ in Eq. 7 is made by averaging the radiances of nearby cirrus-free pixels (as determined by a pre-computed cloud mask) on a land-water-background basis. Figure 9 illustrates graphically the process of retrieving cirrus emissivity and temperature. Effective particle size is tied to temperature, and also varies throughout the iteration process.

In Figure 9 are plots of all mathematically possible pairs of cirrus temperature and emissivity for a given set of satellite radiance observations. The radiance observations correspond to an MWIR brightness temperature of 273 K, and a TIR temperature of 265 K. Note that for a single wavelength the number of theoretically possible pairs (ε,T) is infinite. This ambiguity is resolved, however, by choosing the retrieved pair as that which satisfies satellite radiance observations at two infrared wavelengths simultaneously. This forms the fundamental basis of our retrieval paradigm.
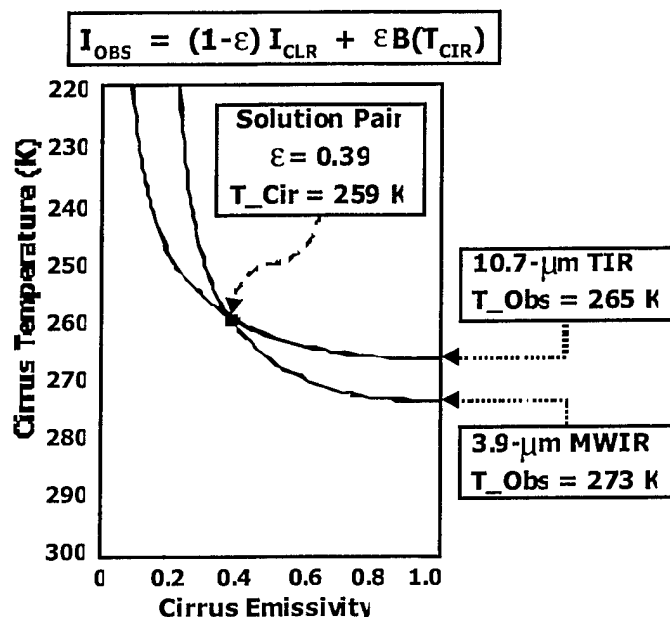
$$I_{OBS} = (1-\varepsilon)\,I_{CLR} + \varepsilon\,B(T_{CIR})$$

Figure 9 Coupled retrieval paradigm

Figure 10 contains a plot of GOES WV-TIR retrievals of cirrus emissivity and altitude superimposed on collocated ground-based 35-GHz radar observations of the same cirrus deck. Time of radar observation is on the x-axis, and on the y-axis are cirrus effective altitude (left) and TIR emissivity (right). Warm colors (red, yellow, orange) in the plot denote stronger radar returns and therefore cirrus clouds that are relatively optically thick. Cool colors (green, blue, cyan) denote weaker returns and therefore optically thinner cirrus. Yellow squares represent satellite-based retrievals of cirrus emissivity, and are to be compared with the TIR emissivity axis on the right. Note in a qualitative sense that the emissivity trace follows the radar trace: relatively high cirrus emissivity is retrieved where radar returns are strong, and vice versa.

Cirrus effective altitude retrievals are represented in Figure 10 by red diamonds, and are to be compared directly with the vertical positions of the radar returns that denote cloud base and top. Note that the red diamonds always fall within the observed positions of the cirrus clouds. The white circles denote retrievals of cirrus temperature that make no allotment for the transmissive nature of the clouds (i.e., the blackbody assumption). Note this is the assumption made in many retrieval schemes including those used operationally by the Air Force Weather Agency in their RTNEPH and CDFS II cloud models. From the figure it can be seen that the blackbody assumption can lead to large cloud altitude retrieval errors. This is due to the fact that the upwelling radiation measured by the satellite from cirrus cloud is a mixture of both cold cloud and warm surface radiation.

The blackbody assumption prescribes that the upwelling radiance is emitted entirely by the cloud, tending to underestimate its altitude in the retrieval. The degree to which the underestimation occurs is a function of the cirrus emissivity. Note first that our coupled cirrus retrievals of emissivity and height (via temperature) always lie above the blackbody retrievals, and are more representative of cloud top. Note too that for the thinner parts of the cirrus (cool colors in the radar returns) the blackbody altitudes often fall completely below the observed bases of the cirrus cloud. This illustrates convincingly the strength of coupling emissivity and temperature in our cirrus retrieval paradigm.
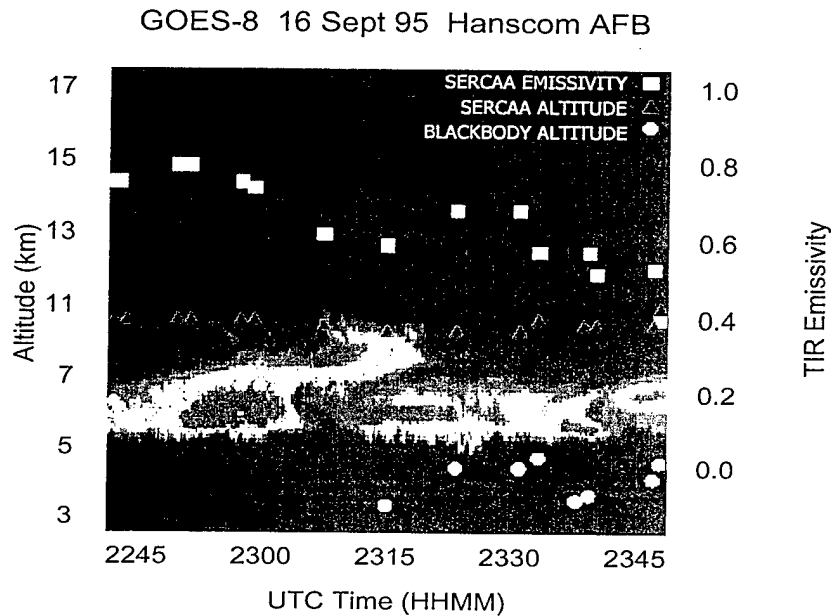

Figure 10 GOES cirrus water-vapor-band retrievals

5. AFRL Contrail Program Support

As described above, the cloud cover/layer algorithm heritage is extensive. Although the new algorithm modules have not yet received the same extensive real-world testing as the heritage algorithms, we did perform considerable testing using MAS, AVHRR and GOES data. Results indicate improved performance over the CDFS II algorithms in the anticipated areas including:

- detection and accurate classification of transmissive cirrus day and night;
- nighttime detection of maritime stratus, fog, and low cloud that are thermally indistinct from the background surface;
- daytime discrimination of cloud over snow and ice backgrounds; and
- cloud phase determination.

38

In support of the AFRL contrail program, two sets of GOES data collected over New England in 1995 and over Florida in 1996, were processed through the cloud detection and property retrieval algorithms. Figure 11 shows the region of interest for the 1995 campaign. GOES data were processed from 25 August and 18-29 September 1995 for the region indicated. In addition, statistical summaries of the cloud products were computed over the grids indicated on the figure. Summary statistics were also computed for the smaller boxes shown in the figure, these correspond to the location of coincident radiosonde measurements. The required information included: Location, amount and height of high and transmissive cloud; Spatial distribution; Radiative properties; Temperature and humidity profiles. In addition to the cloud products, GOES sounder data were processed to provide pixel-level vertical profiles for temperature and humidity. For each of the boxes in Figure 11, the following information was provided:

- presence of cloud with a top altitude of greater than 9 km (representing cloud at contrail altitudes);

- presence of cloud with a 10.8-μm emissivity of less than 0.5 (representing transmissive cloud);

- mean height and frequency distribution of all heights of clouds in the region with top altitudes greater than 9 km;

- mean height and frequency distribution of all heights of clouds in the region with 10.8-μm emissivity less than 0.5;

- presence of cloud with a top altitude of less than 9 km (representing cloud below altitude of interest for contrail study);

- fractional cloud amount over the region for cloud with top altitudes greater than 9 km;

- fractional cloud amount over the region for cloud with top altitudes less than 9 km;

- mean, maximum and minimum of 6.7-μm raw satellite counts and brightness temperatures for all pixels within region (required by contrail prediction algorithm);

- mean, maximum and minimum of 10.8 μm radiance ($Wm^{-2}\mu m^{-1}ster^{-1}$) for all pixels within region (required by contrail prediction algorithm); and

- mean, maximum and minimum of 12.0-10.8 μm brightness temperature difference, and number of pixels with temperature differences greater than 3.5K (required by contrail prediction algorithm).

For the large boxes in Figure 11, the following additional information was provided:

- distance from center of the four boxes to the nearest cloud with a top altitude of greater than 9 km; and

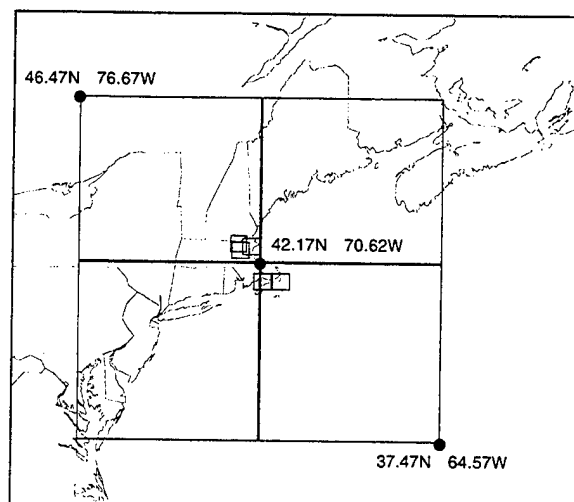- distance from the center of the four boxes to nearest cloud with a 10.8-μm emissivity of less than 0.5.

Figure 11 New England domain for 1995 field program

GOES data for the Florida region of interest were processed over the domain shown in Figure 12 for the period 19-22 September 1996. For this data set the required information included pixel-level retrievals of:

- Cloud effective temperature;

- Cloud top pressure and height;

- IR emissivity and optical depth;

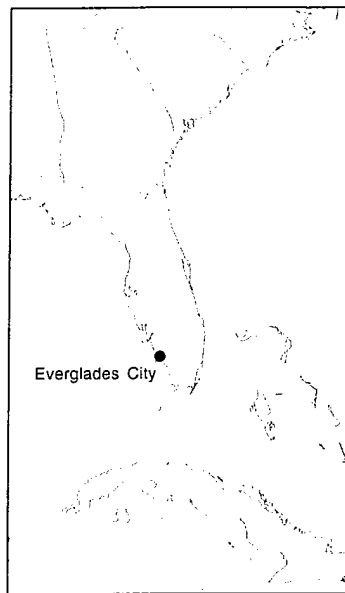- Effective particle size; and

- Ice/liquid water path.

Figure 12 Florida domain for 1996 field program

5.1 Output Products and Display

Figure 13 – Figure 17 contain examples of cirrus retrievals over the northeast U.S. and adjacent Atlantic on 18 Sept 95 at 0245 UTC. The figures demonstrate the ability to process large amounts of data through the software and that results are internally consistent and show good qualitative agreement with the gross meteorological features in the scene. The depicted storm system has an area of deep convection near its center, just east of Maine. There is also an outbreak of convection just ahead of a trailing cold front that is due south of New England, out over the Atlantic and east of the mid-Atlantic states. Figure 13 shows the retrieval of cloud emissivity for the scene and qualitatively demonstrates good agreement with the scene meteorological characteristics, since the retrieved emissivities are high in areas of deep convection where cloud optical depth is expected to be high and lower as the boundary of the cirrus deck is approached. Similarly Figure 14 shows that the cirrus effective cloud-top retrievals in altitude (km) and pressure (mb) space are again consistent with reality in that the highest cirrus is associated with the deepest convection. Figure 15 shows a plot of cirrus effective particle size D_{eff} (μm). In general, ice crystals are smaller when cirrus temperatures (heights) are lower (higher). This is due primarily to decreasing amounts of available water vapor as the ambient air temperature decreases, as described by the Clausius-Clapeyron relation. Figure 16 contains retrievals of ice water path (IWP, g/m^2) as given by Eq. 43, and corresponds well in a qualitative sense with the emissivity retrievals. Finally, Figure 17 contains an image of visible optical thickness retrievals as specified by Eq. 46.
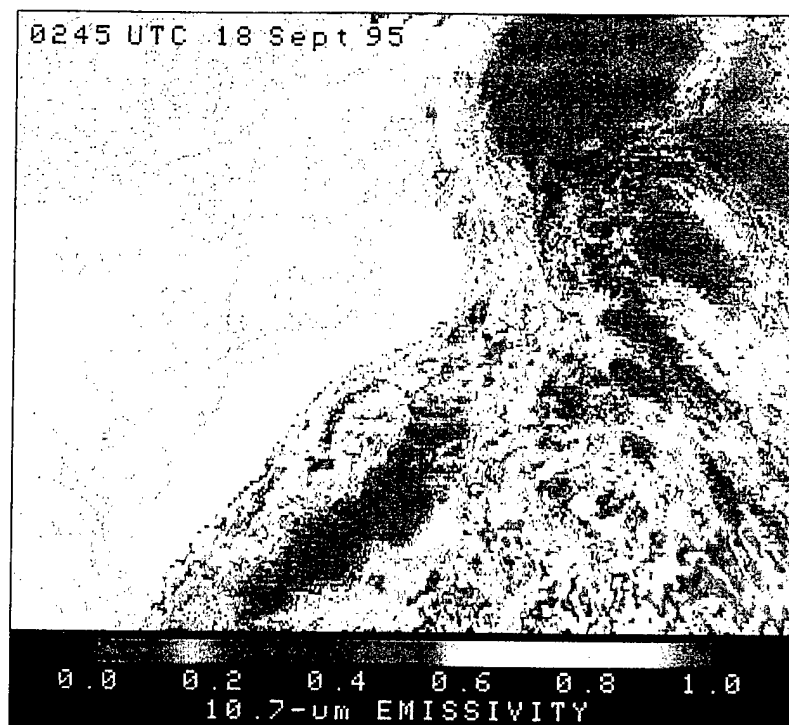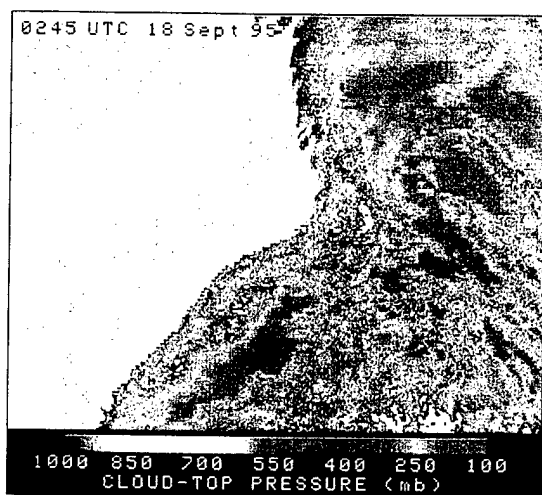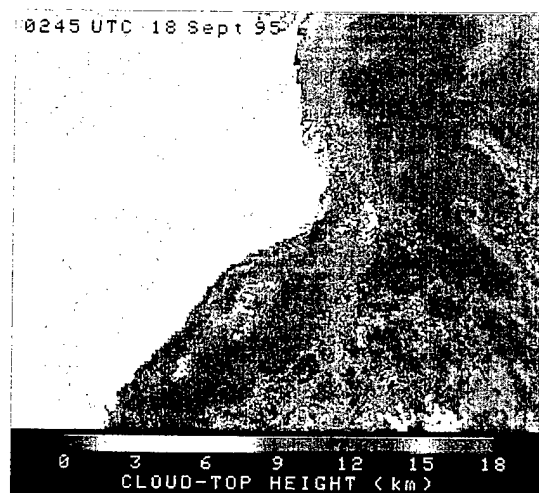
41

Figure 13 Cirrus thermal infrared emissivity

(a)

(b)

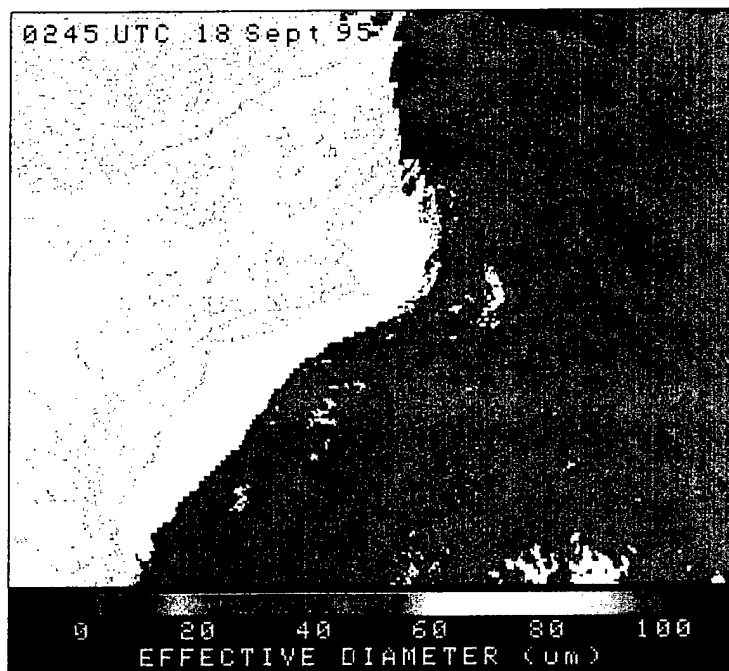**Figure 14 Cirrus effective pressure (a) and altitude (b)**
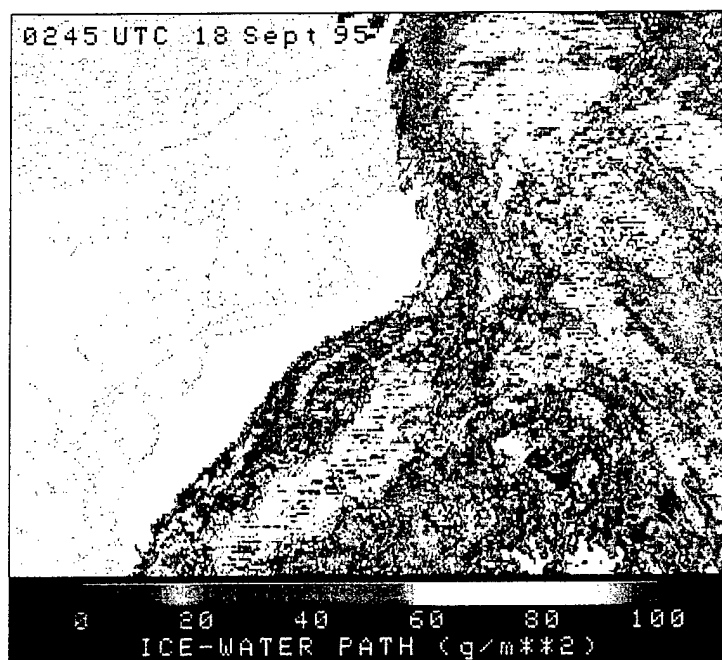
Figure 15 Ice-crystal effective diameter

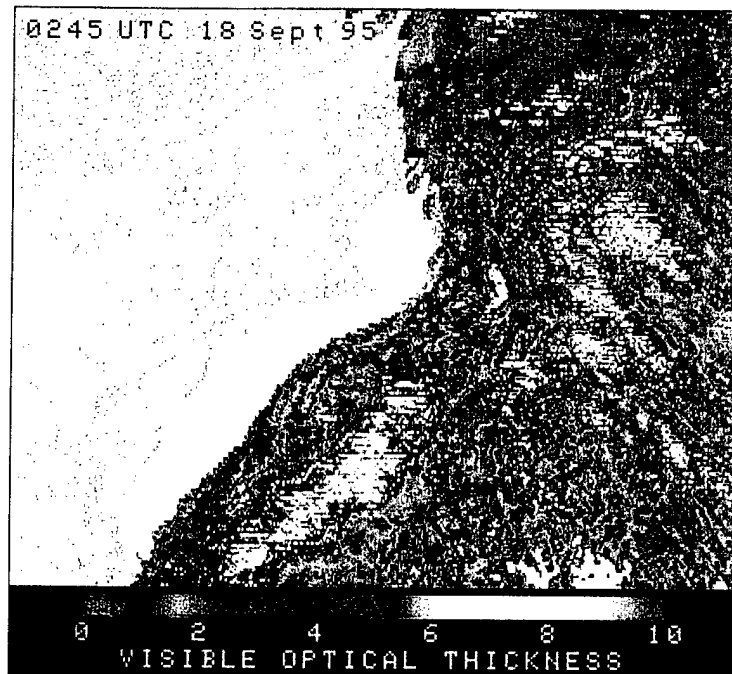**Figure 16 Cirrus ice water path**

43

Figure 17 Cirrus visible optical thickness

6.   Summary

Cirrus spatial (altitude, fraction), radiative (optical thickness, emissivity), and microphysical (particle size, IWP) retrievals are estimated using a deterministic algorithm that simultaneously models the interdependent effects of IWP, ice-particle size, emissivity, and cirrus temperature using radiances collected in nominal 3.9, 6.7, and 10.8-μm infrared wavelengths. The retrieval algorithm uses a simultaneous-solution approach to ensure physical consistency between multispectral satellite radiance measurements and theoretical radiative transfer calculations.

Retrieval results indicate that, in general, cirrus altitude is better estimated using our coupled technique relative to traditional blackbody assumptions and that the improvement in altitude retrievals increases with decreasing cirrus emissivity. As cirrus optical thickness decreases, more and more of the upwelling infrared energy originates from the warmer surface beneath the cloud. Forced to assume that the entirety of upwelling energy is emitted by the cirrus itself, the blackbody assumption tends therefore to overestimate the cirrus temperature, thereby underestimating its altitude. Subsequently the blackbody altitude retrievals, such as those in the RTNEPH and CDFS-II cloud analysis models, are consistently underestimating the altitudes of thin cirrus clouds. This has the effect of placing some very thin cirrus within the atmospheric boundary layer, which in turn manifests itself adversely in subsequent cloud forecasts both from a cloud-height and trajectory perspective. Coupled cirrus altitude retrievals in all likelihood represent the single most noticeable improvement that can be made to Air Force operational analysis- and forecast-model products. It is noted that the sensor channel

44

wavelengths required to operate the coupled cirrus algorithms are currently available to CDFS II and thus any potential upgrade of those algorithms would not impose any additional data constraints on the system.

Cirrus IWP retrievals are a by-product of our coupled algorithm approach. Preliminary sensitivity studies indicate that, in general, IWP is almost always underestimated using our technique and that the magnitude of the underestimation increases with increasing cirrus optical thickness. This is due not so much because of a lack of understanding of the in-cirrus radiative transfer as it is a limitation of the usefulness of thermal infrared data to solely address this problem. Under conditions of very opaque cirrus when infrared IWP retrievals are expected to be poor (but altitude retrievals are expected to be excellent), coincident microwave radiance observations would be of great value in assessing the ice amounts deeper in the cloud. In such instances the infrared radiances would be most sensitive to the small ice crystals near the cloud top. These crystals tend to obscure the underlying parts of the cirrus from view of the IR sensors. However, microwave radiances are minimally sensitive to the small particles near the cirrus top, but increasingly sensitive to the ice mass below as the particle sizes increase. Consequently it is expected that couple microwave-IR radiance observations would complement each other quite well in retrievals of IWP and other cirrus properties, and offers substantive hope for improvements of cirrus optical and radiative properties in the coming years.

7. References

Ackerman, S.A., K.I. Strabala, W.P. Menzel, R.A. Frey, C.C. Moeller and L.E. Gumley, 1998: Discriminating clear sky from clouds with MODIS. *J. Geophys. Res.*, 103, D24, 32,141-32,157.

Ackerman, S.A., K.I. Strabala, W.P. Menzel, R.A. Frey, C.C. Moeller, L.E. Gumley, B.A. Baum, C. Schaaf and G. Riggs, 1997: Discriminating clear sky from cloud with MODIS algorithm theoretical basis document (MOD35), EOS ATBD web site, 125 pp.

Baran, A. J., J. S. Foot, and D. L. Mitchell, 1998: The question of ice crystal absorption: a comparison between T-matrix, Mie and anomalous diffraction theory and implications for remote sensing. *Appl. Optics*, 37, 2207-2215.

Bryant, F. D., and P. Latimer, 1969: Optical efficiencies of large particles of arbitrary shape and orientation. *Journ. Colloid and Interface Sci.*, 30, 291-304.

d'Entremont, R. P., D. P. Wylie, S.-C. Ou, and K.-N. Liou, 1996: Retrieval of Cirrus Radiative and Spatial Properties Using Coincident Multispectral Imager and Sounder Data. *Preprints, Eighth Conf. On Satellite Meteorology and Oceanography*, Amer. Meteor. Soc., 377-381.

d'Entremont, R.P., 1993: Detection and analysis of cirrus clouds using passive infrared satellite data. *Proceedings, Passive Infrared Remote Sensing of Clouds and the Atmosphere*, 13-15 April, 1993, Orlando, FL. SPIE, 1934, 164-179.

Deirmendjian, D., 1969: *Electromagnetic scattering on spherical polydispersions*. Elsevier, New York.

Francis, P. N., J. S. Foot, and A. J. Baran, 1999: Aircraft measurements of the solar and infrared radiative properties of cirrus and their dependence on ice crystal shape. *Journ. Geophys. Res.*, 104, 31685-31695.

Gustafson, G.B., R.P. d'Entremont and M. Hoefer, 2000: Hourly global cloud property retrievals from DMSP, TIROS, and geostationary EO sensors. *Preprints, Tenth Conf. On Satellite Meteorology and Oceanography*, Amer. Meteor. Soc., 126-129.

Gustafson, G.B., R.G. Isaacs and B. McDonnald, 1997: The cloud depiction and forecast system II nephanalysis model. *Preprints, Cloud Impacts on DoD Operations and Systems*. Newport, RI, 119-122.

Gustafson, G.B., R.P. d'Entremont and R.G. Isaacs, 1996: Support of environmental requirements for cloud analysis and archive (SERCAA): final report. PL-TR-96-2224, Phillips Laboratory, Hanscom AFB, MA, 71 pp.

Gustafson, G.B., R.G. Isaacs, J.M. Sparrow, D.C. Peduzzi and J.S. Belfiore, 1994: Automated satellite cloud analysis – tactical nephanalysis (TACNEPH). PL-TR-94-2160, Phillips Laboratory, Hanscom AFB, MA, 99 pp.

Gustafson, G.B., R.G. Isaacs, R.P. d'Entremont, J.M. Sparrow, T.M. Hamill, C. Grassotti, D.W. Johnson, C.P. Sarkisian, D.C. Peduzzi, B.T. Pearson, V.D. Jakabhazy, J.S. Belfiore, and A.S. Lisa, 1994: Support of Environmental Requirements for Cloud Analysis and Archive (SERCAA): Algorithm Descriptions. TR-94-2114, Phillips Laboratory, Hanscom AFB, MA, ADA 283240, 100 pp.

Gustafson, G.B. and G.W. Felde, 1989: Validation of automated cloud detection from microwave imagery. Preprints: *5th Conference on Interactive Information Processing Systems*, American Meteorological Society, Boston, MA, 379-386.

Hale, G. M., and M. R. Querry, 1973: Optical constants of water in the 200-nm to 200-μm wavelength region. *Appl. Optics,* 12, 555-563.

Heideman, K.F., J.M. Sparrow and T.S. Lisa, 1984: Validation of the SERCAA cloud analysis algorithm. Preprints, *7ᵗʰ Conference on Satellite Meteorology and Oceanography,* American Meteorological Society, Boston, MA, 326-329.

Heymsfield, A. J., 1986: Ice particles observed in a cirriform cloud at –83 °C and implications for polar stratospheric clouds. *J. Atmos. Sci.,* 43, 851-855.

Hunt, G. E., 1973: Radiative Properties of Terrestrial Clouds at Visible and Infra-Red Thermal Window Wavelengths. *Quart. Journ. Royal Meteor. Soc.,* 99, 346-369.

Karlsson, K.G. and E. Liljas, 1990: The SMHI model for cloud and precipitation analysis from multispectral AVHRR data. PROMIS Report No. 10, Swedish Meteorological and Hydrological Institute, Norrkoping, Sweden. August 1990, pp. 74.

Knollenberg, R. G., K. Kelly, and J. C. Wilson, 1993: Measurements of high number densities of ice crystals in the tops of tropical cumulonimbus. *J. Geophys. Res.,* 98, 8639-8664.

Mace, G. G., T. P. Ackerman, P. Minnis, and D. F. Young, 1998: Cirrus layer microphysical properties derived from surface-based millimeter radar and infrared interferometer data. *Journ. Geophys. Res.,* 103, 23207-23216.

Matrosov, S. Y., 1999: Retrievals of vertical profiles of ice cloud microphysics from radar and IR measurements using tuned regressions between reflectivity and cloud parameters. *Journ. Geophys. Res.,* 104, 16741-16753.

McFarquhar, G. M., and A. J. Heymsfield, 1996: Microphysical characteristics of three anvils sampled during the central equatorial pacific experiment. *Journ. Atmos. Sci.,* 53, 2401-2423.

Miles, N. L., J. Verlinde, and E. E. Clothiaux, 2000: Cloud droplet size distributions in low-level stratiform clouds. *J. Atmos. Sci.,* 57, 295-311.

Mitchell, D. L., and W. P. Arnott, 1994: A model predicting the evolution of ice particle size spectra and radiative properties of cirrus clouds. Part II: Dependence of absorption and extinction on ice crystal morphology. *Journ. Atmos. Sci.,* 51, 817-832.

Mitchell, D. L., 1996: Use of mass- and area-dimensional power laws for determining precipitation particle terminal velocities. *Journ. Atmos. Sci.,* 53, 1710-1723.

Mitchell, D. L., A. Macke, and Y. Liu, 1996: Modeling cirrus clouds. Part II: treatment of radiative properties. *Journ. Atmos. Sci.,* 53, 2967-2988.

Mitchell, D. L., 2000: Parameterization of the Mie extinction and absorption coefficients for water clouds. *Journ. Atmos. Sci.,* 57, 1311-1326.

Ou, S. C., K. N. Liou, W. M. Gooch, and Y. Takano, 1993: Remote Sensing of Cirrus Cloud Parameters Using Advanced Very High Resolution Radiometer 3.9- and 10.9-μm Channels. *Appl. Optics,* 32, 2171-2180.

Saunders, R.W. and K.T. Kriebel, 1988: An improved method for detecting clear sky and cloudy radiances from AVHRR data. *Int. J. Remote Sens.,* 9, 123-150.

Slingo, A., 1989: A GCM parameterization for the shortwave radiative properties of water clouds. *Journ. Atmos. Sci.,* 46, 1419-1427.

Sparrow, J.M., G.B. Gustafson, R.G. Isaacs, J.T. Bunting and R.P. d'Entremont, 1993: Validation of infrared cloud detection algorithms developed for TACNEPH.

Proceedings, Passive Infrared Remote Sensing of Clouds and the Atmosphere, 13-15 April, 1993, Orlando, FL. SPIE, 1934, 62-71.

Stowe, L.L., P.A. Davis and E.P. McClain, 1999: Scientific basis and initial evaluation of the CLAVR-1 global clear/cloud classification algorithm for the advanced very high resolution radiometer. *J. Atmos. Oceanic Tech.*, 16, 656-681.

Strabala, K.I., S.A. Ackerman and W.P. Menzel, 1994: Cloud properties inferred from 8–12-μm data. *J. Appl. Meteor.*, 33, 212-229.

Stubenrauch, C. J., R. Holz, A. Chedin, D. L. Mitchell, and A. J. Baran, 1999: Retrieval of cirrus ice crystal sizes from 8.3 and 11.1- μm emissivities determined by the improved initialization inversion of TIROS-N Operational Vertical Sounder observations. *J. Geophys. Res.*, 104, 31,793-31,808.

Takano, Y., K.N. Liou and P. Minnis, 1992: The effects of small ice crystals on cirrus infrared radiative properties. *Journ. Atmos. Sci.*, 49, 1487-1493.

Takano, Y. and K.N. Liou, 1989: Solar Radiative Transfer in Cirrus Clouds. Part I: Single Scattering and Optical Properties of Hexagonal Ice Crystals. *Journ. Atmos. Sci.*, 46, 3-19.

Van de Hulst, H. C., 1981: Light Scattering by Small Particles. Dover, 470 pp.

8.   Acronym List

ADA	Anomalous Diffraction Approximation
AVHRR	Advanced Very High Resolution Radiometer
CDFS II	Cloud Depiction and Forecast System II
DMSP	Defense Meteorological Satellite Program
EBBT	Equivalent Blackbody Brightness Temperature
FOV	Field Of View
GOES	Geostationary Operational Environmental Satellite
LWIR	Long Wave Infrared wavelength
MAS	MODIS Airborne Simulator
MODIS	Moderate resolution Imaging Spectroradiometer
MWIR	Mid Wave Infrared wavelength
NIR	Near Infrared wavelength
NWP	Numerical Weather Prediction
RTNEPH	Real Time Nephanalysis
SWIR	Short Wave Infrared wavelength
TIR	Thermal Infrared wavelength
TIROS	Television Infrared Observing System
VIS	Visible wavelength
WV	Water Vapor absorption band wavelength